DEVELOPMENT OF A THICK GAS ELECTRON MULTIPLIER DETECTOR FOR MICRODOSIMETRY

DEVELOPMENT OF A THICK GAS ELECTRON MULTIPLIER DETECTOR FOR MICRODOSIMETRY

By

GLORIA M. ORCHARD, M.SC., B.SC.

A Thesis

Submitted to the School of Graduate Studies

in Partial Fulfillment of the Requirements

for the Degree

Doctor of Philosophy

McMaster University

DOCTOR OF PHILOSOPHY (2010) McMaster University

(Medical Physics) Hamilton, Ontario

TITLE: Development of a Thick Gas Electron Multiplier Detector for Microdosimetry

AUTHOR: Gloria M. Orchard (née Spirou), M.Sc. (University of Toronto), B.Sc. (York University)

SUPERVISOR: Dr. Soo-Hyun Byun

NUMBER OF PAGES: xv, 121

Abstract

In experimental microdosimetry one of the goals is to measure the absorbed dose in microscopic volumes of tissue. The traditional spherical tissue-equivalent proportional counter (TEPC) is the most common detector currently used for microdosimetry. A new microdosimetric detector based on a thick gas electron multiplier (THGEM) was developed. To investigate the feasibility of the THGEM type detector for microdosimetry, a prototype detector was designed and manufactured. The THGEM detector is robust, easy to manufacture and is cost effective. The THGEM foil is composed of a thin FR4-epoxy insulator coated with copper on both sides. The THGEM contains 32 holes each with a diameter of 0.35 mm and pitch of 0.64 mm. The sensitive volume of the detector is a right cylinder with a diameter of ~ 5 mm and height of ~ 5 mm and is located in the center of the detector. Systematic tests were conducted at the McMaster Accelerator Laboratory to investigate its overall performance. A neutron-gamma ray radiation field was generated using the ^{7}Li(p,n) reaction. The detector was operated at low bias voltages initially to test the stability and then the relative multiplication gain was measured as a function of the operating high voltage. The detector performance was observed with different THGEM insulator thicknesses ranging from 0.12 mm to 1.48mm. The multiplication gain was assessed and both neutron and gamma-ray radiation was detected by the THGEM detector. The spectra obtained with the THGEM detector were analyzed and compared to the data collected with the standard spherical TEPC. The investigations provided information about the THGEM detector operation for microdosimetry and the THGEM microdosimetric spectra observed are comparable to the standard TEPC data.

Acknowledgements

I would like to thank my committee members, Drs. William Prestwich, David Chettle, Fiona McNeill and Anthony Waker. Their knowledge and guidance during my doctoral studies provided me with support, not only about my studies, but about life in general. This work would not have been possible without Kenrick Chin and Jason Falladown. The seemingly endless THGEMs were fabricated by Kenrick, and he never questioned why I kept breaking them. To Jason, thank you for running the Tandetron accelerator and for the long conversations and encouragement to figure things out when the THGEM detector would stop working. Most of all, none of this would have happened if it was not for the never ending support of my supervisor, Dr. Soo-Hyun Byun. Byun, your endless positive energy kept me going and you always noted the bright side of everything. Your knowledge of microdosimetry and detectors continues to amaze me!

Four years at McMaster led to many unforgettable friendships. In particular, I want to remember Michael Chamberlain. I never got the chance to let you know how much you influenced my graduate life. His charming smile, amazing stories and passion for life kept me afloat during the down times. He is, and will always be, greatly missed. To all my office mates, Amanda Fice, James Grafe and Eric Da Silva it was great sharing stories and long discussions instead of just office space.

To my parents, family and friends, especially Cristina and Robyn, for always supporting me and encouraging me to never give up. Thank you for always being there for me.

Finally, to my husband and best friend, Trevor, who never doubted me and always stood by my side. His continuous love and support reminds me how lucky we are to have found each other. The birth of our daughter, Sofia, in 2009, gave me the strength I needed to finish my PhD and has given life a new meaning. I love you both very much - *Σας αγαπω παρα παρα πολυ.*

Table of Contents

List of Figures

List of Tables

Chapter 1

Experimental Microdosimetry

1.1 Introduction

In experimental microdosimetry, the main goal is to measure the absorbed dose as a spectrum of individual energy depositing events in microscopic volumes of tissue (Waker, 1995). Different types of ionizing radiation can lead to different biological effects. This is related to the linear energy transfer (LET) associated with different types of ionizing radiation and the level of biological detriment and is quantified using the relative biological effectiveness (RBE) for a given radiation (ICRU, 1983). The LET can be related to the distribution of the dose. The ability of microdosimetry to separate different LET components is very useful for medical applications and radiation protection (Waker, 1995). The biological effects depend on the pattern in which a given amount of energy is deposited in the irradiated medium. Low pressure tissue equivalent proportional counters (TEPCs) are a versatile tool in radiation physics, radiation protection and radiation biology, and are used to measure the absorbed dose spectrum in microscopic tissue volumes. The traditional spherical TEPC is the most common detector currently used for microdosimetry. A TEPC can simulate microscopic

volumes of tissue and is used for microdosimetry studies (Waker, 1995; Rossi and Zaider, 1996; Byun, 2007a). In this thesis, a new type of TEPC based on a thick gas electron multiplier (THGEM) for microdosimetry is presented and compared to the traditional spherical TEPC.

1.2 Microdosimetric Quantities

When energy is transferred to a microscopic volume, the amount of energy transferred can fluctuate. Thus, the energy transferred to the mass of the microscopic volume is a statistical quantity referred to as the specific energy, z. The specific energy, z refers to the energy, ε imparted to mass, m of the irradiated volume of interest. The SI unit of z is energy in Joules [J] per mass in kilograms [kg] which is represented by the gray [Gy = J/kg].

$$z = \frac{\varepsilon}{m} \tag{1.1}$$

The lineal energy, y is defined as the absorbed energy in a volume by a single energy deposition event divided by the mean chord length, $\bar{l}$. The SI unit for y is the [J/m] but most commonly [keV/μm] is used in experimental microdosimetry. Similarly to the specific energy, lineal energy is also a stochastic quantity.

$$y = \frac{\varepsilon}{\bar{l}} \tag{1.2}$$

The mean chord length, $\bar{l}$ represents the geometrical mean length of randomly oriented chords in the irradiated volume. In general $\bar{l}$ in random transversal of a volume is 4 V/S where V is the volume and S is the surface area of that volume (Rossi and Zaider, 1996). For spherical and right cylindrical volumes the mean chord length is:

$$\bar{l} = \frac{2d}{3} \tag{1.3}$$

where d is the diameter of the sphere or right cylinder.

Over a large volume the mean specific energy, $\bar{z}$ is the expectation value of the specific energy probability distribution ($f(z)$) of specific energy events:

$$\bar{z} = \int_0^\infty z f(z) dz \tag{1.4}$$

The mean specific energy is a non-stochastic quantity and is equal to the absorbed dose D. D is defined as the average energy absorbed per unit mass of irradiated medium. For a finite volume we can obtain the absorbed dose by measuring the total energy absorbed, E_{total} [J] and dividing by the mass, m [kg] of the irradiated volume. The unit of D is also the Gy.

$$D = \frac{E_{total}}{m} \tag{1.5}$$

Given the microdosimetric definitions presented in equations (1.1) to (1.5) the relationship between single energy deposition events and the measured absorbed

dose is described. Using this known relationship the absorbed dose can be measured in experimental microdosimetry. (Rossi and Zaider, 1996; ICRU, 1983)

1.3 Microdosimetric Spectrum

In microdosimetry there is a standard representation of displaying the information detected by a TEPC. The microdosimetric spectrum is represented by plotting the lineal energy on a logarithmic scale on the horizontal axis with the vertical axis displaying the event distribution multiplied by the corresponding lineal energy. The dotted line in Figure 1.1 depicts the standard representation of a microdosimetric spectrum. This spectrum was measured by a TEPC exposed to a mixed neutron-gamma radiation field generated by 2.0 MeV protons with a current of 200 μA accelerated onto a lithium (^{7}Li) target. One of the advantages of microdosimetry is the ability to separate the different LET components when a mixed radiation field is used. As shown in Figure 1.1, the neutron (dashed line) and gamma-ray (solid line) components of the radiation field can be separated. The gamma-ray component of the radiation field shown in Figure 1.1 can be obtained by reducing the proton beam energy to 1.8 MeV which is below the neutron reaction threshold value. In the mixed radiation field displayed in Figure 1.1, the known gamma spectrum of Cesium-137 (^{137}Cs) is used to display the entire gamma-ray spectral shape expected. The ^{137}Cs spectrum has a gamma-ray energy spectral shape that is similar to the generated spectrum of the gamma-ray

radiation of the mixed field used to obtain the spectrum shown Figure 1.1. The energy deposition of the low energy gamma rays is undetected as the pulse height generated by these events is near or below the electronic background noise of the detector and associated pulse processing components. The mixed field is separated by obtaining the spectrum of the gamma-rays independently of the neutrons and subtracting this gamma-ray spectrum from the spectrum obtained with a mixed neutron-gamma radiation field under the same experimental conditions. This standard representation of a microdosimetric spectrum is beneficial as the area under the spectrum is related to the absorbed dose, *D*.

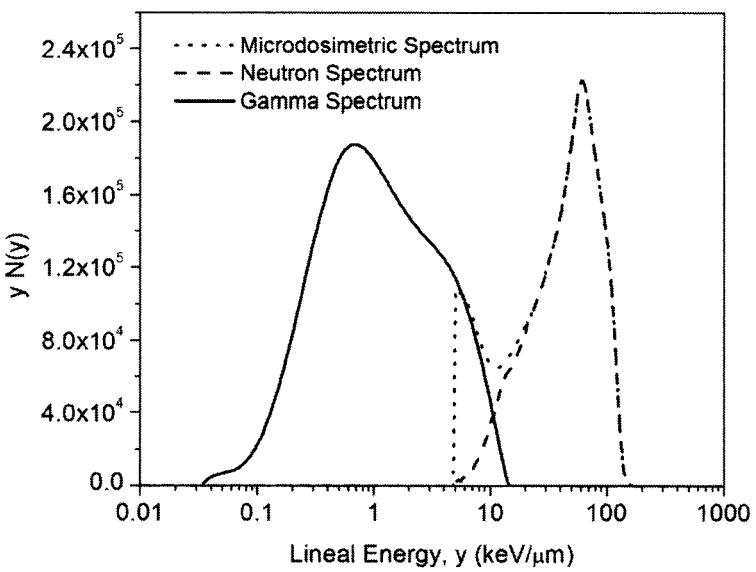

Figure 1.1: Standard representation of a microdosimetric spectrum. The horizontal axis displays the lineal energy, y (keV/μm) on a logarithmic scale and the vertical axis is proportional to the absorbed dose. The dotted line is the microdosimetric spectrum measured with a spherical TEPC, the solid line is the expected gamma ray spectrum and the dash line represents the neutron spectrum. The neutron spectrum is obtained by subtracting the measured gamma spectrum from the total measured spectrum.

1.4 Radiation Source

The Tandetron accelerator neutron source at the McMaster Accelerator Laboratory was used as the radiation source (Byun *et al.,* 2007a). The neutron source has been mainly used for medical and radiobiological applications. A thick lithium (Li) target is installed in the proton beam path and produces an intense neutron field through the ^{7}Li(p,n) reaction. The threshold proton energy for the ^{7}Li(p,n) reaction is 1.88 MeV and a suitable proton energy is selected depending on the application. The raw neutron spectrum from the lithium target is a broad continuous spectrum in the hundred keV region and the maximum neutron energy increases with increasing proton energy (Matysiak, Prestwich and Byun, 2008; Lee and Zhou, 1999). An irradiation cavity has been placed around the lithium target, as shown in Figure 1.2, and can be used to irradiate either a human hand for *in vivo* activation analysis of trace elements accumulated in bone or a small animal for radiobiology studies (Byun *et al.,* 2007a). A competing ^{7}Li(p,p'γ) reaction produces 478 keV gamma rays, and 2.2 MeV gamma rays are also produced from the ^{1}H(n,γ) reaction due to the presence of the polyethylene moderator.

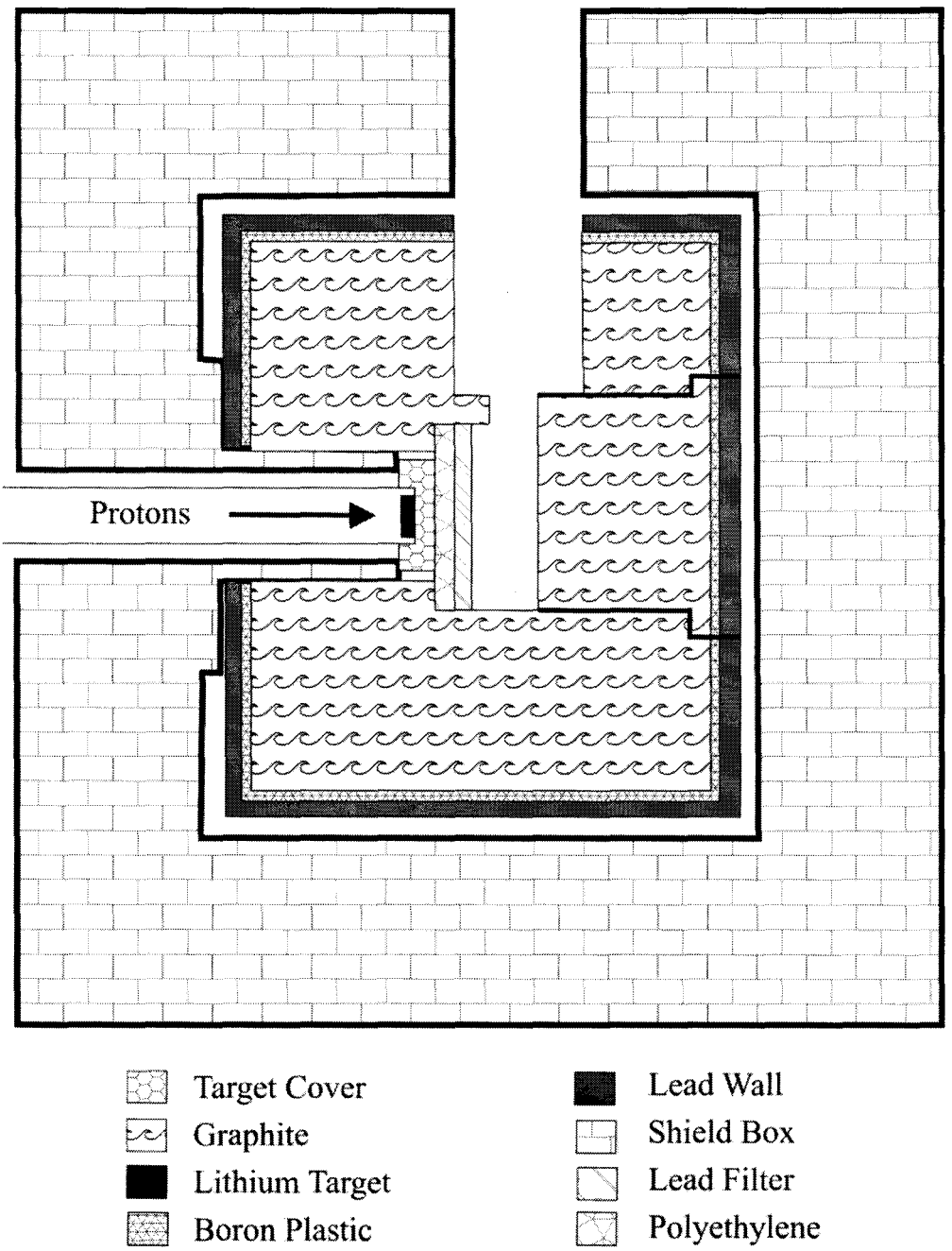

Figure 1.2: Cross section schematic diagram of the irradiation cavity used at the Tandetron accelerator neutron source. The shield box is made of cooperate (a mixture invented by Alan Cooper, Department of Nuclear Physics, Australian National University and is composed of polyethylene beads, boron and resin).

As described in Section 1.3, one of the advantages of microdosimetry is the ability to separate different LET components. In this case, the radiation field contains both gamma-rays and neutrons. By knowing the properties of the generated field in the irradiation cavity the two components can be separated. The gamma-ray field shape can be obtained by setting the proton energy below the ^{7}Li(p,n) reaction threshold (< 1.88 MeV). Once a pure gamma-ray spectrum is obtained the two fields can easily be separated and the dose contribution from the different radiation types can be obtained. However, a significant fraction is attenuated by the lead filter located behind the moderator. The irradiation cavity is well shielded to minimize the streaming radiation (Byun *et al.*, 2007a). In the studies presented in Chapters 3, 4 and 5, reference to the proton energy, E_p and current, I_p refers to the proton beam parameters.

1.5 Radiation Interactions

Using a TEPC the expected dose to human tissue within the irradiation cavity can be measured by obtaining the microdosimetric spectrum as described in Section 1.3. The dose is measured as the incoming radiation deposits energy within the sensitive volume of the detector which simulates a microscopic tissue volume. As described in Section 1.4 the source of the radiation in this case is from a broad energy spectrum of neutrons and two gamma ray energies. Both neutrons and gamma rays are indirectly ionizing radiation. Indirectly ionizing

radiation generates secondary charged particles, which in turn deposit energy within the irradiated region (Hall and Giaccia, 2006). The sensitive volume of the detector contains tissue equivalent (TE) gas which is composed of hydrogen, carbon, nitrogen and oxygen. The radiation interacts with the detector wall or gas particles to generate charged particles, which then deposit their energy to the surrounding medium as they are slowed down. As a result, electron-ion pairs are produced along the track of the charged particle. The collection of the electrons is used to accumulate the microdosimetric spectrum and measure the absorbed dose.

1.5.1 Sensitive Volume

The sensitive volume of the proportional counter encompasses the volume where interactions of the incident radiation with the gas molecules can occur. The sensitive volume contains the desired gas and is the region where ion pairs are generated indirectly from the incoming radiation. In microdosimetry the sensitive volume of the proportional counter is filled with tissue equivalent (TE) gas at a pressure which simulates a small volume of biological tissue. The sensitive volume is also used for gas multiplication and thus the geometry of the detector is important. In order to achieve the most uniform gas multiplication, multiplication should be confined to a very small region compared to the total sensitive volume and should occur as close to the anode as possible (Kliauga *et al.*, 1995; Knoll, 2000).

1.5.2 Tissue Simulation

The amount of electron-ion pairs generated within the detector sensitive volume must equal the same number of electron-ion pairs that would be created in the track in the actual tissue volume of interest. In order to simulate biological tissue using TE gas, the energy deposition of the incident radiation within the TE gas must be identical to the energy deposition within a real microscopic size volume of tissue. The energy deposition within tissue, E_t can be expressed as the product of the tissue mass stopping power, the tissue density and the path length across the tissue volume (Waker, 1995):

$$E_t = \left(\frac{1}{\rho}\frac{dE}{dx}\right)_t \rho_t \Delta x_t \tag{1.6}$$

Similarly, the energy deposited by a charged particle crossing the detector gas volume, E_g is expressed as (Waker, 1995):

$$E_g = \left(\frac{1}{\rho}\frac{dE}{dx}\right)_g \rho_g \Delta x_g \tag{1.7}$$

where in equations (1.6) and (1.7) the symbols represent:

E – energy deposited
$\left(\frac{1}{\rho}\frac{dE}{dx}\right)$ – mass stopping power
ρ – density
Δx – path length across volume
t – tissue
g – gas

Given the mass stopping power of tissue and TE gas are the same (a gas property requirement in order to simulate tissue using TE gas) the energy deposited in tissue and the gas medium must be the same, $E_t = E_g$. Thus, equating equations (1.6) and (1.7) the relationship between tissue volume being simulated and TE gas within the detector is (Waker, 1995):

$$\rho_t \Delta x_t = \rho_g \Delta x_g \tag{1.8}$$

The values of Δx_g and Δx_t correspond to the diameter of the sensitive volume to be filled with TE gas and the diameter of the microscopic tissue volume to be simulated, respectively. From equation (1.8) the density of the gas, ρ_g required to simulate the desired tissue volume can be calculated. This condition can be achieved by filling the sensitive volume with the appropriate TE gas pressure. The gas pressure, P_g required to simulate the desired microscopic tissue volume can be obtained using the ideal gas law:

$$P_g = \rho_g \frac{RT}{M} \tag{1.9}$$

where R is the ideal gas constant (8.31 J mol^{-1} K^{-1}), T is the temperature and M is the molecular mass of the TE gas.

1.5.3 Neutron Interactions

When neutrons interact with the TE gas molecules within the detector, charged particles within the sensitive volume are indirectly generated. The generated particles are produced through nuclear interactions, and elastic or

inelastic collisions. The kerma is used to describe the energy imparted per unit mass by charged particles, which are generated by interactions with neutrons. Figure 1.3 is a plot of the kerma coefficient as a function of neutron energy for the elements hydrogen (^{1}H), carbon (^{12}C), oxygen (^{16}O), and nitrogen (^{14}N) which are found in TE gas. The figure displays the kerma for the elemental composition of TE propane gas and includes the neutron kerma for TE propane gas, which is the gas used to fill the detectors presented in this research. The elemental neutron kerma coefficients were obtained from Chadwick *et al.* (1999). The elemental composition of TE propane gas is 10.3 % ^{1}H, 56.9 % ^{12}C, 29.3 % ^{16}O and 3.5 % ^{14}N (ICRU, 1983).

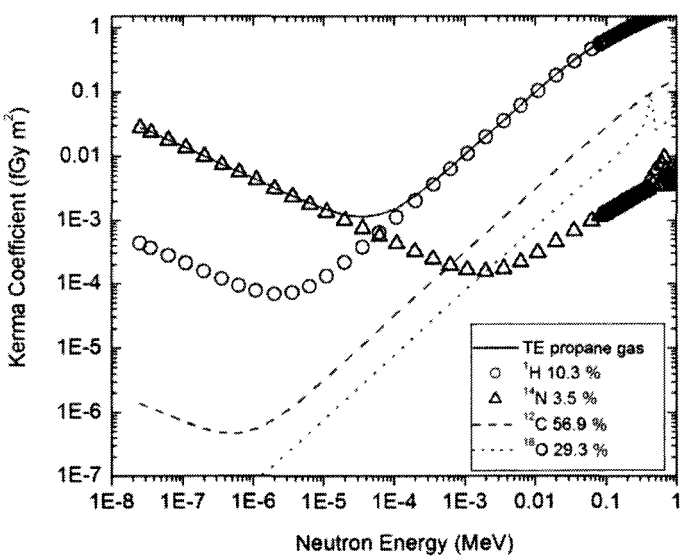

Figure 1.3: Kerma coefficients for neutrons with energies from thermal to 1 MeV on the elemental composition of TE propane gas and TE propane gas. The dominant interactions of neutrons with the TE gas occur with the hydrogen and nitrogen components (Chadwick, 1999).

These charged particles traverse the sensitive volume and deposit their energy along a track by generating electron-ion pairs. Due to the nature of neutron interactions, a range of charged particles with their own energy spectrum and interaction properties are created within the sensitive volume (Waker, 1995). In the energy range of neutrons generated by the radiation source described in Section 1.4 the dominant interactions of generated charged particles occur through the $^{14}N(n,p)^{14}C$ reaction and elastic scattering of the neutrons with the TE gas molecules. According to Figure 1.3 the dominant interactions of the neutrons occur with the nitrogen and hydrogen components of the TE propane gas. The nitrogen component dominates at the thermal neutron energies (~ 0.025 eV) and at the higher energies, the hydrogen component of the gas is dominant due to elastic scattering.

1.5.4 Gamma Ray Interactions

The primary interaction of gamma rays with the sensitive volume of the detector is Compton scattering. Compton scattering is an inelastic interaction between the incident photons and electrons in the absorbing medium. As a result, Compton electrons are released as the secondary charged particles. It is the energy of these secondary electrons that is deposited within the sensitive volume (the TE gas) of the detector (Waker, 1995). In Compton scattering the scattering angle is variable and thus the secondary electrons generated contain a broad energy spectrum.

1.5.5 Energy Deposition Distribution within the Sensitive Volume

The direction of the charged particles crossing the detector volume can limit the available track length for energy deposition within the sensitive volume. Thus the amount of energy deposited by the charged particle within the sensitive volume is variable. The energy imparted within the cavity of the detector by each particle can be classified into four types: "insiders", "starters", "stoppers" and "crossers" (ICRU, 1983). Particles originating in the volume and depositing their entire energy in the volume are classified as "insiders" while "starters" refers to particles that originate in the volume but exit the volume without depositing all their energy. "Stoppers" includes particles that originate outside the sensitive volume and enter and then stop within the volume. Finally, "crossers" refers to all particles that originate outside the sensitive volume but cross the volume and deposit part of their energy in the volume. In other words, the maximum energy of the charged particles is deposited only when the entire track of the electron-ion pairs are generated within the sensitive volume. Furthermore, the maximum lineal energy measured by the detector corresponds to the energy deposition along the largest length of the sensitive volume (Waker, 1995).

1.6 Detectors for Microdosimetry

There are limited available detectors for microdosimetry. The most common detector is a commercially available 0.5-inch diameter spherical TEPC

(Far West, Inc.). Although this is a standard detector for microdosimetry there are some limitations associated with the design. The spherical TEPC, as the name implies, is composed of a spherical cavity with an anode along the diameter. In order to maintain constant multiplication throughout the anode a helix electrode is introduced around the anode. These are the basic components of the spherical TEPC but additional components such as the anode wire support system are required to hold all the components in place (Kliauga *et al.*, 1995). Braby *et al.* (1995) provide an extensive description of the mechanical design of a spherical TEPC and indicate the complicated processes required to fabricate the relevant components for small size spherical TEPCs. For intense radiation fields, due to higher count rates pulse pile up and large dead time issues arise, requiring a reduced size spherical TEPC (i.e. < 0.5-inch diameter) for such measurements. Reducing the size of the spherical TEPC design requires all components to be smaller and a thinner anode wire is required. Fine wires (diameter < 2.5 μm) become harder to work with and air currents can make positioning this wire within the TEPC very difficult (Braby *et al.* 1995).

The concept of a proportional counter using a hole type structure has been studied since the mid 1990's with a strong research interest continuing today. Some early references include Sakurai *et al.* (1996) and F. Sauli (1997). A common name for this type of proportional counter is the gas electron multiplier (GEM) and it is composed of a thin sheet of insulator which is coated on both

sides with a conducting material, such as copper (^{64}Cu). The GEM also contains a two-dimensional array of microscopic holes that allow a strong electric field to be generated within them when a voltage is applied across the conducting layers. Depending on the strength of the electric field generated across the holes, electron multiplication can be observed when electrons are accelerated through these holes. A proportional counter (PC) based on a capillary plate was reported by Sakurai *et al.* (1996). The capillary plate proportional counter described by Sakurai *et al.* (1996) was filled with a gas mixture of argon + 5 % methane and was used to investigate the performance when exposed to ^{55}Fe (Iron) 5.9 keV x-rays. The capillary plate consists of a bundle of fine glass capillaries, each capillary with a diameter and length of 100 μm and 800 μm, respectively. Gas multiplication occurs within the capillaries when a voltage difference is applied across the plate similar to the GEM holes. In their studies they presented the detector stability, relative gain as a function of applied voltage and a pulse height distribution of the ^{55}Fe source. Dubeau *et al.* (2000) designed a TEPC based on the microstrip gas counter (MSGC). The MSGC contains alternate anode and cathode metal strips etched on a resistive substrate. In their study the anodes were 7 μm wide and the cathodes were 80 μm wide. The spacing between adjacent anodes was 200 μm. An electric field is generated when a voltage difference is applied between the anodes and cathodes and gas multiplication is generated between neighbouring strips (Oed, 1988). The small dimensions of the MSGC

are attractive for microdosimetry, but the electric field generated for gas multiplication between adjacent anode and cathode is within the sensitive volume of the detector. One of the advantages of the GEM is the multiplication region is separate from the sensitive volume of the detector, which is ideal to ensure consistent multiplication. The studies presented by Farahmand *et al.* (2003) and Dubeau and Waker (2007) focussed on designing a TEPC based on a GEM. Farahmand *et al.* designed a cylindrical type detector with the GEM placed at the bottom of the cylinder parallel to the circular cross section. The detector was constructed with TE materials and contained a cylindrical gas filled cavity where electron-ion pairs are generated prior to gas multiplication through the GEM holes. Initial microdosimetric measurements with this detector were reported by Farahmand *et al.* in 2004. Their results showed good agreement with spectra from the literature collected with the currently available TEPC, and reported the relative simple design and construction of the detector and the components are adaptable to meet the required needs. Additionally, Dubeau and Waker (2007) investigated a TEPC based on the GEM for the use as an electronic personal dosimeter. The dimensions of the active area of the detector are 7 cm x 7 cm with a thickness of ~ 2 mm with a readout pattern consisting of 128 strips. They reported on the response of the detector to a range of neutron fields with results indicating the detector may be a good base for a personal neutron dosimeter.

More recently, the thick GEM (THGEM) has emerged which is a larger version of the GEM. The THGEM contains a thicker insulating layer and larger diameter holes compared to the standard GEM. Compared with the GEM, the THGEM is easier to manufacture and is cost effective. It was first introduced in 2002 by Periale *et al.* and initial studies were reported in 2003 (Periale *et al.*, 2003; Ostling *et al.*, 2003). Further studies and advances on the THGEM and applications have been reported and continue to be investigated (Chechik *et al.*, 2004, 2005; Shalem *et al.*, 2006a, 2006b; Oliveira *et al.*, 2007; Di Mauro *et al.*, 2007; Peskov *et al.*, 2007; Cortesi *et al.*, 2007). The capillary plate, MSGC and GEM are all gas multiplication devices and seem to be ideal choices for proportional counters and have been studied for microdosimetry applications.

In this thesis a new type of TEPC based on the THGEM will be introduced and described, along with initial experimental results and comparison with the standard TEPC. The motivation of investigating the THGEM detector for microdosimetry includes the easy fabrication, robustness and cost effectiveness relative to spherical and GEM based TEPCs. Also, the versatility of the THGEM has the potential to develop miniature detectors for measurement of intense radiation fields and two-dimensional imaging.

The research presented in this thesis can be divided into four parts. Chapter 2 describes the physical and functional characteristics of the THGEM TEPC and the spherical TEPC detectors for microdosimetry studies. The main

focus of this chapter is on the THGEM type detector design, as the goal of this thesis is to characterize and analyze the THGEM TEPC function and compare the results with the commercially available spherical TEPC (which will be referred to as the standard TEPC in this thesis). Chapter 3 describes and compares the three available pulse processing systems used to obtain the microdosimetric spectra with the two detectors. In Chapters 4 and 5 the experimental results of the THGEM detector will be reported. Finally, a discussion of all the results along with conclusions and future work will be presented Chapter 6.

Chapter 2

Microdosimetry Detectors

2.1 Detectors for Microdosimetry

A proportional counter is the type of detector commonly used for microdosimetry (Waker, 1995; Rossi and Zaider, 1996). In this chapter two proportional counters will be described. Briefly a commercially available spherical tissue-equivalent proportional counter (TEPC) will be presented followed by a detailed description of the thick gas electron multiplier (THGEM) detector design for microdosimetry. A general description of proportional counters will provide the basic concepts for both detectors.

2.1.1 Proportional Counters

Proportional counters are gas-filled detectors and were first introduced in the late 1940's. Two electrodes, an anode and a cathode, are separated by a region referred to as the sensitive volume which is filled with gas. Radiation interacts with the gas molecules within the sensitive volume and surrounding wall materials, and generates electron ion pairs. An electric field is applied to induce gas multiplication which is used to amplify the charge represented by the original ion pairs created by irradiation of the gas. Gas multiplication in a proportional

counter is an ideal way of detecting the small number of ion-pairs generated by the incoming radiation which is very useful in microdosimetry. For uniform multiplication to be achieved, the gas multiplication region must be confined to a very small volume (near the anode) compared to the sensitive volume. When a sufficient electric field is applied, the electron-ion pairs generated by the incident radiation drift toward their respective electrodes, electrons toward the anode and ions toward the cathode. As free electrons move toward the anode by the applied electric field they may collide with other neutral gas molecules and generate additional free electrons. As long as the electric field is above the threshold field value all free electrons generated by collisions will be accelerated and generate additional ionizations as they move towards the anode. As a result a cascade, known as the Townsend Avalanche, of electrons is formed due to the gas multiplication. The avalanche is terminated when all the free electrons are collected at the anode of the proportional counter. The main advantage of a proportional counter, under proper operating conditions, is the average number of secondary ionization events is proportional to the primary ion pairs formed. Since the primary ion pairs formed deposit their energy in the gas, the total charge of the number of secondary electrons collected at the anode is directly proportional to the energy deposited by the incident radiation. (Knoll, 2000)

2.1.2 Tissue Equivalent Materials

In order to fabricate a TEPC the active volume of the detector must be composed of mainly tissue equivalent (TE) materials. The TE materials for the detectors presented in this research contain A-150 plastic and Rexolite 1422 (Rexolite 1422, C-LEC Plastic Inc.). A-150 plastic is a conducting plastic and was originally developed by Shonka and is composed of polyethylene, nylon, carbon black, magnesium oxide and calcium fluoride (Braby *et al.*, 1995). Rexolite 1422 (hereafter rexolite) is an insulating plastic and composed of cross linked polystyrene (C-LEC Plastics, 2010). Additionally, the gas used within the proportional counter must also be tissue equivalent in order to simulate a tissue equivalent environment. As described in Section 1.5 the detectors were filled with TE propane gas which is composed of 55% propane (C_3H_8), 39.5% carbon dioxide (CO_2) and 5.5% nitrogen (N_2).

2.1.3 Absorbed Dose

The data accumulated from a TEPC can be used to obtain the absorbed dose within the sensitive volume. The absorbed dose is related to the area under the microdosimetry spectrum as described in Section 1.3. Once the spectrum is calibrated and displayed in the standard representation, the absorbed dose rate can be calculated. The calculation details to obtain the measured dose rate are presented in Chapter 3.

2.2 Spherical TEPC

The spherical TEPC used in this research was provided by Far West Technology, Inc. (Model LET-1/2) and was used to obtain the standard microdosimetric spectrum that was then used to validate the data obtained with the THGEM detector. The spherical TEPC, as in the name, contains a 1.27 cm diameter spherical cavity, surrounded by a 0.127 cm thick TE A-150 plastic. The TEPC was filled with propane based TE gas at 66.4 torr which simulates a 2 μm diameter soft tissue spherical volume with a density of 1 g/cm^3. An anode wire transverses the diameter of the cavity and a helical grid surrounds it to generate an even electric field along the anode wire. A voltage of 580 V was applied to the cathode and 80 V was supplied to the helical grid. As electrons are attracted towards the anode, due to the larger electric field strength gas multiplication occurs mainly between the grid and the anode, thus maintaining the ideal conditions for gas multiplication near the anode. Figure 2.1 (a) is a schematic diagram of the spherical TEPC and (b) is a diagram of the spherical cavity and the radiation interactions. The incoming ionizing radiation generates secondary particles which then transverse the gas cavity and generate electron ion pairs. The electric field within the cavity drifts the electrons towards the anode where electron multiplication occurs between the helical grid and the anode.

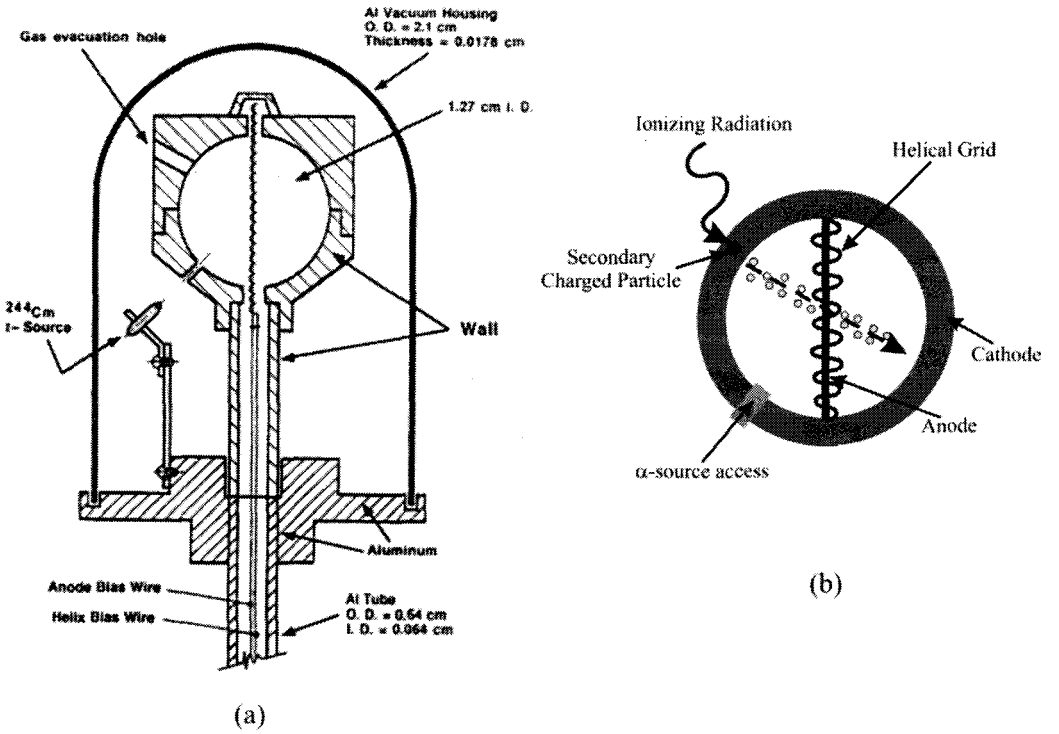

Figure 2.1: (a) Schematic drawing of a spherical TEPC used for microdosimetry (Langen *et al.*, 2002). (b) Cross section diagram of spherical cavity components and radiation interactions. The outer gray circle represents the A-150 plastic wall and the inner cavity is filled with TE gas, where energy is deposited from the secondary charged particles generated due to the radiation interaction with the wall.

The spherical TEPC contains an internal calibration alpha source used to calibrate the lineal energy of the detected radiation interactions. The calibration source is ^{244}Cm (curium) and has a mean alpha energy of 5.80 MeV, which corresponds to an average lineal energy of 127 keV/μm over a 2 μm diameter volume of tissue. The internal ^{244}Cm source was used to calibrate the spectra obtained with the spherical TEPC. Once calibrated the lineal energy of the

neutron peak measured with the spherical TEPC was used to calibrate the THGEM detector data.

2.3 THGEM Detector

The overall volume of the THGEM detector assembly is 5 cm x 5 cm x 1 cm and is housed in an aluminum casing. The materials used for the components include a THGEM, TE conducting plastic (A-150), TE insulating plastic (rexolite) and a collection plate used as the anode. Additionally, there are electrical wires and resistors used to provide the required voltages to the THGEM. In this section, the design of the THGEM detector will be presented first, followed by the THGEM fabrication, the THGEM electric field and electron multiplication, the collection plate (anode), detector assembly and lastly, the robustness of the detector will be discussed.

2.3.1 Detector Design

As wall materials, both tissue equivalent conductors and insulators were used to simulate a tissue equivalent environment surrounding the sensitive volume as shown in Figure 2.2 (a cross section schematic of the detector). The two A-150 plastic conducting components have dimensions of 50 x 50 x 1.9 mm. The thick rexolite component has dimensions of 50 x 50 x 4.9 mm and the thin rexolite piece is 50 x 50 x 0.25 mm. A 5 mm diameter hole is drilled through the centre of both rexolite components to create the sensitive volume within the thick

rexolite while the gap generated in the middle of the thin rexolite piece allows for the collection of the emerging electrons from the THGEM. The sensitive volume created by the hole drilled in the thick rexolite component is a right cylinder with a diameter of ~ 5 mm and height of ~ 5 mm and is located in the centre of the detector assembly.

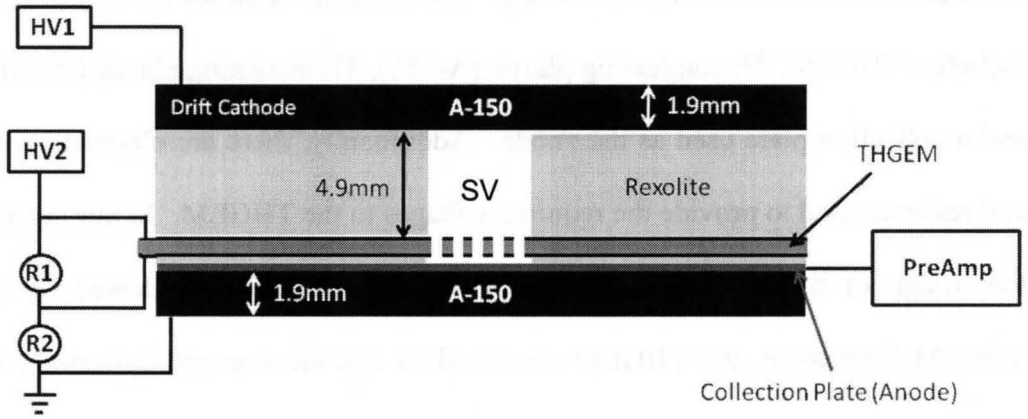

Figure 2.2: Cross section schematic of the THGEM TEPC. (Figure is not to scale; actual THGEM thickness is ~ 0.24 mm.) The sensitive volume (SV) is filled with TE propane gas. HV1 is used to supply voltage to the drift cathode and HV2 is used to supply voltage across the THGEM to create the electric fields for electron multiplication and collection.

As shown in Figure 2.2, the THGEM is placed between the two rexolite pieces which are located between the two A-150 TE plastic components. The thin layer of rexolite placed between the THGEM and collection plate (anode) separates the THGEM from the anode which collects the electrons once they emerge from the THGEM holes. Two narrow gas flow channels located on the top

and bottom of the 4.9 mm thick rexolite wall allow for pumping and filling of the sensitive volume (SV).

The high voltage (HV) connections are also displayed in Figure 2.2. A dual high voltage supply with two independent outputs is used to set the desired high voltage values for HV1 and HV2 (Model 3125, Canberra). Each output can provide positive or negative voltage with a range of 0 – 5000 V. For the THGEM detector negative HV values were applied. The drift cathode (A-150 plastic) was biased independently using HV1 while the top and bottom surfaces of the THGEM were biased from a common bias supply, HV2, which is divided by a factor using resistors $R1$ and $R2$. The electrons are collected after the multiplication process with a collection plate (anode), which is DC coupled to a preamplifier. ΔV_{Drift} is used to denote the voltage difference between the drift cathode and the top of the THGEM.

$$\Delta V_{Drift} = HV2 - HV1 \tag{2.1}$$

The HV2 voltage applied to the detector ranged from -500 V to -1340 V. The voltage, HV1, applied to the drift cathode was always maintained at least 100 V more negative than HV2, thus $\Delta V_{Drift} \geq 100$ V.

The resistors $R1$ and $R2$ are chosen such that most of the voltage is applied across the THGEM and the remainder is used to direct the electrons to the collection plate. In the data presented here a resistance of 10 MΩ for $R1$ was used

while the $R2$ value was maintained at approximately one tenth of $R1$. As a result the voltage across the THGEM, ΔV_{THGEM} is equal to:

$$\Delta V_{THGEM} = \frac{\Delta V \times R1}{(R1 + R2)} \tag{2.2}$$

where ΔV is the change in voltage between HV2 and ground as shown in Figure 2.2. Analogously, the voltage across the bottom of the THGEM and the collection plate, ΔV_{CP} can be calculated using:

$$\Delta V_{CP} = \frac{\Delta V \times R2}{(R1 + R2)} = \Delta V - \Delta V_{THGEM} \tag{2.3}$$

2.3.2 THGEM

The THGEMs were fabricated using an FR4-epoxy sheet coated with copper on both sides. The size of each THGEM was 5 cm x 5 cm with a varying thickness ranging from 0.26 mm to 1.54 mm. All THGEMs contain 32 holes each with a diameter of (0.35 ± 0.01) mm and pitch of (0.64 ± 0.03) mm located in the middle of the foil. A micro drill was used to create the THGEM holes in the centre of the sheet and two micrometers were used for positional accuracy. THGEMs with different insulator thicknesses were made ranging from 0.12 – 1.48 mm. Figure 2.3 (a) is a picture of a fabricated THGEM and (b) is a microscopic view of the THGEM holes. The holes located in the corners of the THGEM were used to hold the foil in place within the detector aluminum casing

and thus the copper near the corners of the THGEM was etched away to eliminate charge flow between the overlapping components after assembly.

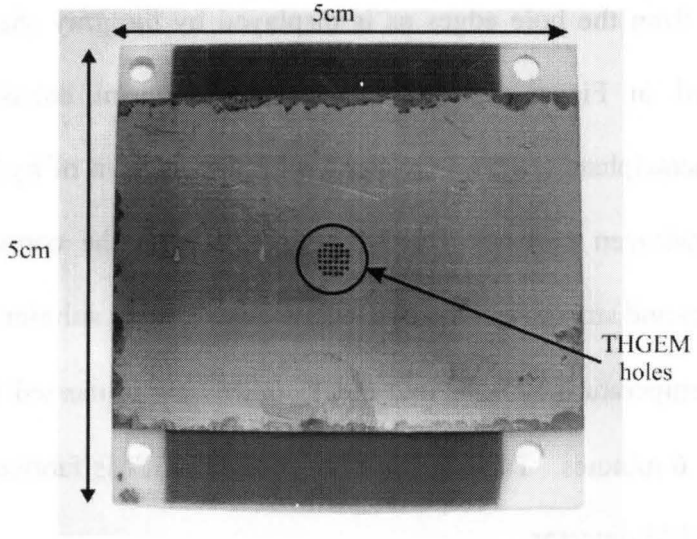

(a)

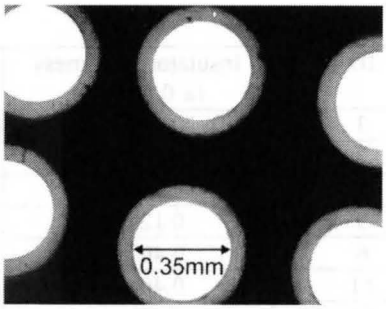

(b)

Figure 2.3: Picture of fabricated THGEM. (a) The holes are centred in the middle of the 5 cm x 5 cm sheet which overlaps with the cylindrical cavity of the detector sensitive volume where electrons are generated and accelerated towards the THGEM holes. The holes located at the corners of the foil are used to hold the THGEM in place within the aluminum casing. (b) Microscopic view of the THGEM holes.

After the drilling of the holes is completed, the THGEM is placed in an etching solution to clean all the holes and remove any sharp copper edges and debris that may be generated during the drilling process. Also, the copper is etched away from the hole edges as is displayed by the gray shade around the holes pictured in Figure 2.3 (b). A standard etchant solution containing ammonium persulphate $(NH_4)_2S_2O_8$ along with the addition of hydrochloric acid (HCl) and hydrogen peroxide (H_2O_2) is used to etch the copper away from THGEM holes and smooth out the hole edges. The etching solution is clear and is heated to a temperature of 80°C and the THGEMs are immersed in the solution for about 4 – 6 minutes. Table 2.1 is a list of all THGEMs fabricated and tested with the THGEM detector.

Table 2.1: A list of the THGEMs used within the THGEM detector, along with the insulator and total thickness measured values.

THGEM	ID	Insulator Thickness (± 0.02 mm)	Total Thickness (± 0.02 mm)
A	3	0.12 mm	0.26 mm
	7	0.12 mm	0.26 mm
	8	0.12 mm	0.25 mm
	9	0.12 mm	0.27 mm
B	6	0.40 mm	0.54 mm
	11	0.40 mm	0.54 mm
	14	0.40 mm	0.53 mm
	15	0.40 mm	0.54 mm
C	5	0.70 mm	0.80 mm
D	16	1.48 mm	1.68 mm

2.3.3 THGEM Electric Field and Electron Multiplication

When a voltage is applied across the THGEM foil an electric field is generated within the THGEM holes. The electric field generated within the THGEM holes was numerically analyzed using the software Maxwell SV 2D (Ansoft, 2004). As expected, the electric field generated within each THGEM hole increases from the centre towards the edge of that hole. Figure 2.4 displays the geometry and electric field profile of a cross section along the diameters of the THGEM holes.

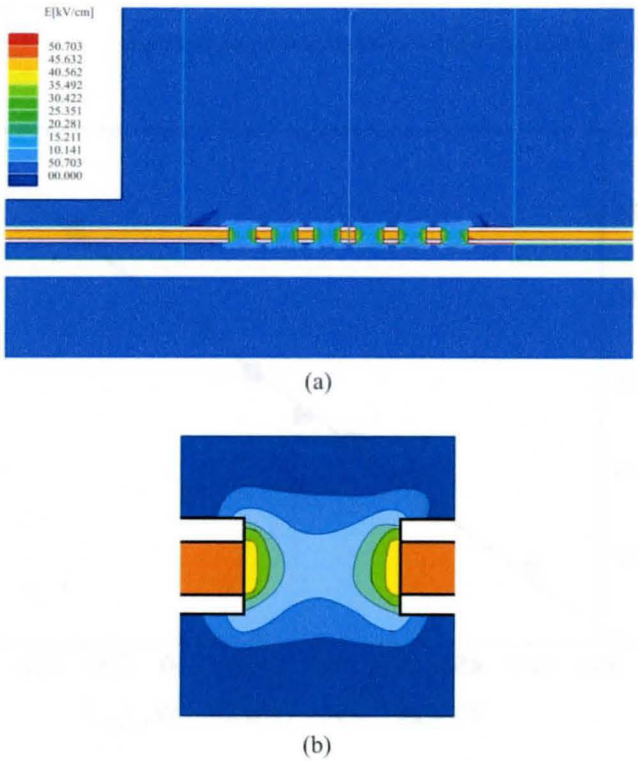

Figure 2.4: Electric field profile within THGEM holes numerically analyzed by MAXWELL SV 2D software. (a) is a cross section of six THGEM holes along the centre of the hole diameters and (b) is a close up of the electric field profile within the hole.

The geometry represents a cross section across the diameter of the sensitive volume of the THGEM detector, which corresponds to the middle of the THGEM foil. This cross section of the THGEM includes 6 holes each with a diameter of 0.35 mm and a pitch of 0.64 mm. The Maxwell calculations were used to obtain the electric field within the THGEM holes for variable ΔV_{THGEM} values. The expected trend is a linear increase in electric field as a function of ΔV_{THGEM}. Figure 2.5 is a graph of the maximum electric field value along the central axis of the THGEM holes as a function of ΔV_{THGEM} as computed by Maxwell. A linear relationship as expected is observed.

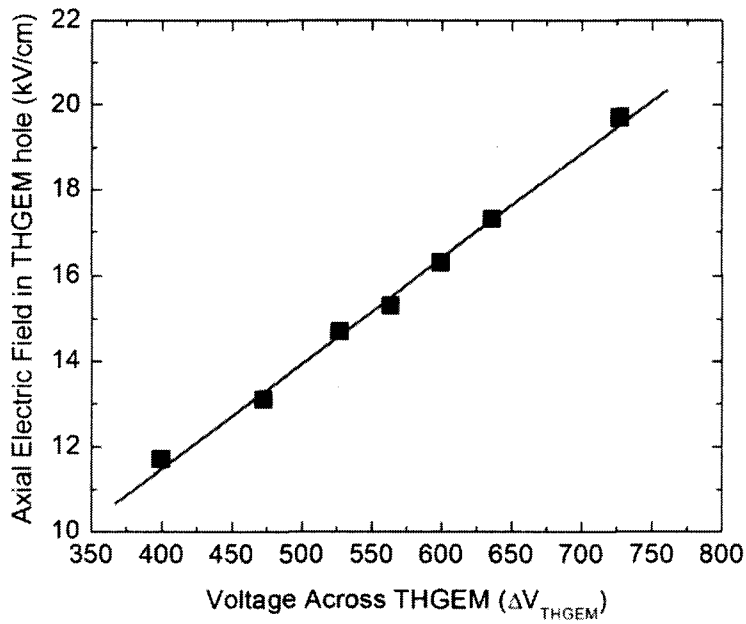

Figure 2.5: The maximum electric field value calculated by Maxwell as a function of increasing voltage across the THGEM, ΔV_{THGEM}. The value of the electric field corresponds to the maximum field calculated along the central axis of the THGEM holes.

Given the electric field generated within the THGEM holes is above the threshold field value required for electron multiplication an avalanche will be generated. A study using the Garfield code was conducted by Byun *et al.* (2009) to simulate the multiplication gain and systematically investigate the dependence of the gain on the THGEM design parameters. Figure 2.6 is a picture of the electron multiplication generated within the THGEM holes as simulated by the Garfield code. The electron multiplication simulation was conducted for a THGEM with a 0.9 mm thickness and a hole diameter of 0.6 mm.

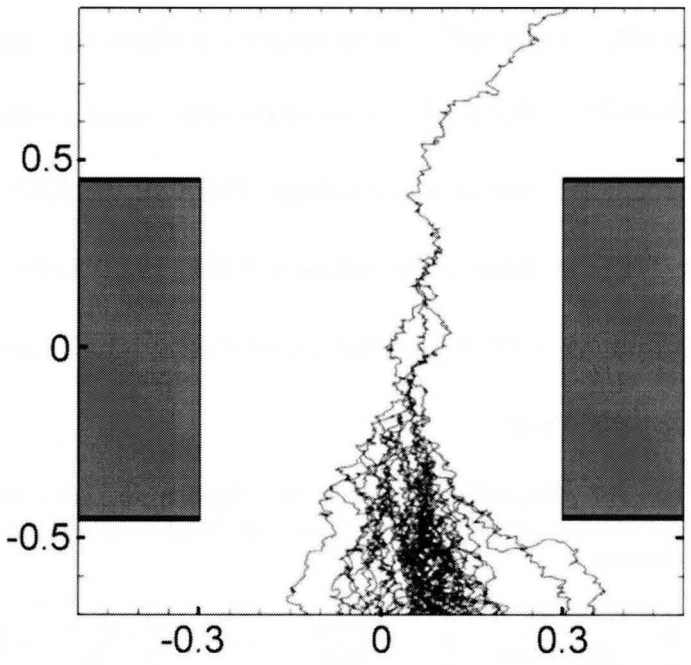

Figure 2.6: Electron avalanche simulation for a THGEM foil with 0.9 mm thickness and 0.6 mm hole diameter. A THGEM bias voltage of 1200 V was used in the simulation. (Byun *et al.* 2009)

2.3.4 The Collection Plate (Anode)

The collection plate or anode is also composed of an FR4-epoxy sheet. A copper strip extending from the middle of the sheet to one of the edges is used as the anode where the electrons are collected. The voltage difference across the bottom of the THGEM and this layer is calculated using equation (2.3) and it is necessary in order to efficiently collect the charges emerging from the THGEM holes. Three different resistors for $R2$ were used to observe the effects of ΔV_{CP} on signal acquisition by the collection plate. It was observed that the range of 70 - 100 V for the potential difference between the bottom of the THGEM and the collection plate (ΔV_{CP}) was sufficient to collect the electrons emerging from the bottom of the THGEM. Table 2.2 is a list of the three resistor values used for $R2$ and the corresponding range of ΔV_{CP} values. From all the HV2 and $R2$ values tested with the THGEM detector the values of 1 MΩ and 0.87 MΩ for $R2$ with a range of ΔV_{CP} from 45 – 77 V provided the best experimental results as will be presented in Chapters 4 and 5.

Table 2.2: The range of voltage difference across the collection plate ΔV_{CP} obtained depending on the resistor value $R2$ and voltage difference ΔV as calculated using equation (2.3). The value of $R1$ was always 10 MΩ.

ΔV (V)	$R2$ (MΩ)	ΔV_{CP} (V)
500 – 1060	0.47	22 – 48
500 – 1240	0.87	40 – 98
500 – 850	1.00	45 – 77
850 – 1100	1.33	100 – 129

2.3.5 Detector Assembly

All the detector components including the inside of the aluminum casing are cleaned using ethanol and assembled in the order as shown in Figure 2.2. Figure 2.7 is a picture of the detector within the aluminum casing. The top black component visible in the picture corresponds to the drift cathode in Figure 2.2.

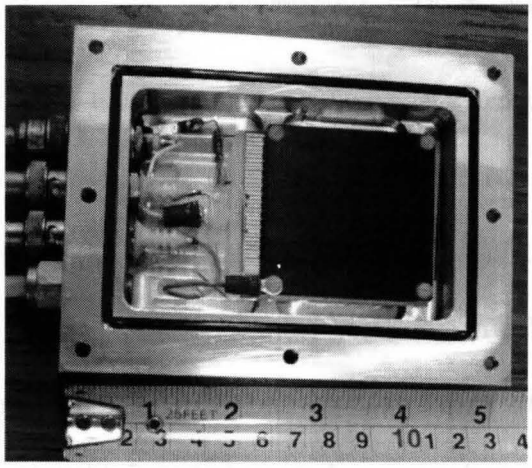

Figure 2.7: Picture of THGEM TEPC detector within the aluminum casing. The visible square black component corresponds to the A-150 plastic (drift cathode) of Figure 2.2.

Once the detector components are cleaned and assembled, they are sealed and connected to a vacuum pump to remove as much of the trapped air as possible. Generally, the detector is evacuated to a pressure below $1x10^{-5}$ torr, requiring at least two days of pumping. After pumping, the detector is filled with TE propane gas at a pressure of 167 torr which simulates a 2 μm diameter right cylinder of unit density soft tissue within the sensitive volume of the detector. The pressure is calculated using the ideal gas law (equation (1.9)) and given the molecular

mass, M of the TE propane gas is constant, the pressure can be calculated using the known pressure, $P_{g\ 20℃}$ = 750.1 torr and density, $\rho_{g\ 20℃}$ = 1.798 kg/m^3 parameters of TE propane gas at 20°C (ICRU, 1983):

$$M = \left(\frac{\rho_g}{P_g} RT\right)_{at\,2\,\mu m,20°C} = \left(\frac{\rho_g}{P_g} RT\right)_{20°C}$$
$$P_{g\,at\,2\,\mu m,20°C} = \rho_{g\,at\,2\,\mu m,20°C} \frac{P_{g\,20°C}}{\rho_{g\,20°C}} = 167 \text{ torr} \tag{2.4}$$

where the TE propane gas density, $\rho_{g\ at\ 2\mu m}$ = 0.4 kg/m^3 is calculated using equation (1.8) with Δx_t = 2 μm, where ρ_t = 1 g/cm^3 and the detector SV diameter is Δx_g = 0.5 mm. Using equations (1.8) and (2.4) the required pressure of the TE propane gas for different simulated volumes of tissue can be calculated. After the detector is filled with TE propane gas and the required voltages HV1 and HV2 are applied the detector can be exposed to a radiation field and tested.

2.3.6 Robustness of THGEM Detector

The overall fabrication of the detector is robust and easy to assemble and disassemble. The aluminum casing protects and encases all the detector components from the outside environment. The high voltages HV1 and HV2 provide the required voltages to the detector components and when the maximum value of HV2 is surpassed a breakdown in the signal acquisition is observed and electron multiplication ceases. This breakdown only affects the THGEM foil and once the THGEM foil is replaced the detector is functional. During preparation of

the detector, which involves cleaning of the components with ethanol, all the wire connections and the resistors $R1$ and $R2$ are always checked with an ohmmeter to ensure all components are connected as expected.

2.4 Testing the THGEM Detector

In Chapter 3 the signal processing required to test the THGEM detector is presented and in Chapters 4 and 5, a series of experimental results are reported. The ability to test the functionality of the different components within the THGEM detector individually was not feasible resulting in multiple possibilities in loss of signal acquisition. For complete experiments the results were compared to the expected microdosimetric spectrum obtained with the standard spherical TEPC. Unfortunately, for failed experiments many unanswered questions arose and will be discussed in Chapter 6. Overall, the THGEM detector described in this Chapter is a prototype detector which has provided positive results for microdosimetry measurements as will be presented in Chapters 4 and 5, along with a discussion and possible future experiments in Chapter 6.

Chapter 3

Comparison of Three Pulse Processing Systems for Microdosimetry

3.1 Preface

The pulse processing associated with microdosimetry requires post acquisition analysis. In general, the data are acquired as a pulse-height spectrum which then must be converted to a microdosimetric spectrum as described in Section 1.3. Of the three systems described here, the real time system (RTS) is able to display the microdosimetric spectrum during signal acquisition. Having the ability to observe the microdosimetric spectral shape during signal acquisition is very beneficial when testing a new detector such as the THGEM TEPC. The results presented in this chapter demonstrate that the three available pulse processing systems can provide equivalent results. From the results, the ability to confidently use the RTS pulse processing system with the THGEM TEPC was ascertained. Thus, the RTS was used in the THGEM TEPC experimental studies presented in Chapters 4 and 5. The work presented in this chapter was accepted by IEEE Transactions on Nuclear Science in June of 2008 and published in October of 2008 (Spirou *et al.*, 2008). (Spirou is the author's maiden name.)

3.2 Abstract

Three different pulse processing systems coupled to a tissue-equivalent proportional counter were tested in performance for various neutron and gamma-ray dose rates. The three systems used are a conventional analogue system, a real time system and a digital pulse processing system. The Tandetron accelerator at the McMaster Accelerator Laboratory was used to produce a mixed neutron-gamma field via the ^{7}Li(p,n) reaction. The proton energy ranged from 1.8 to 2.5 MeV with the current set at 100, 200 and 300 μA. The digital system displayed the fastest pulse processing speed. Microdosimetric spectra from the three systems were consistent and both neutron and gamma-ray dose rates showed good agreement in most cases. At the neutron dose rates higher than 20 mGy/min, the data from the digital system was reliable while systematic deviations were observed for the other two systems.

3.3 Introduction

To process pulse signals from a TEPC detector, a pulse height analysis system is required. Until now, traditional analog pulse processing has been employed most commonly for microdosimetry. Although digital pulse processing has been widely applied to HPGe and Si(Li) semiconductor detectors, along with recent rapid progress in digital signal processing technology, and has proved to have a superior performance (Scates and Hart, 2005; Reguigui *et al.*, 2002; Vo

and Russo, 2002; Bateman *et al.*, 2000), there are still no reports on its application to TEPC detectors. Hence, a systematic investigation on the application of digital processing for a TEPC detector should be beneficial.

When a conventional pulse height analyzer is employed for a TEPC detector, it is difficult to analyze and display a microdosimetric spectrum in real time and therefore a post spectral analysis is unavoidable. Also, the post analysis is time consuming. Moreover, it disturbs quick identification of quality or important dose components of the radiation field during irradiation. In order to overcome this inconvenience innovatively, a real time analysis system was recently developed by our group (Byun *et al.*, 2007b).

The goal of this study was to investigate and compare the performance of three different pulse processing systems, a conventional analogue system (CAS), a real time system (RTS) and a digital signal processing system (DPP). Depending on the characteristics of the radiation field to which a TEPC detector is exposed, such as dose rate or high LET to low LET dose ratio, one system may be more advantageous than another. To estimate both advantages and limitations clearly, the three systems were tested for various radiation field conditions.

3.4 Materials and Methods

The Tandetron accelerator neutron source (Byun *et al.*, 2007a) described in Section 1.4 at the McMaster Accelerator Laboratory was used for testing the

three pulse processing systems. The spherical TEPC described in Section 2.2 was used to measure the neutron and gamma-ray microdosimetric spectrum for a 2 μm diameter spherical tissue volume. The detector was placed in the irradiation cavity centred on the proton beam axis. The internal ^{244}Cm alpha source of the TEPC was used to calibrate the lineal energy in the pulse height spectrum. The output of the TEPC was connected to a charge sensitive preamplifier (Model 2006, Canberra). All three pulse processing systems were connected in parallel to the preamplifier (Preamp) and operated simultaneously. Figure 3.1 is a schematic diagram showing the setup of the signal processing elements used for the three systems.

In the CAS, the signal from the preamplifier is shaped with a shaping time of 1.0 μs using a spectroscopy amplifier (model 2020, Canberra). The pulse height is then digitized using a successive approximation peak-sensing analog-to-digital converter (ADC) (model 919E, ORTEC). The software Gammavision (ORTEC) was used to collect the pulse height spectrum.

For digital processing, a commercial digital pulse processing system (Model DSPEC, ORTEC) was employed. In this system, a pulse extracted by the preamplifier is directly digitized by a sampling ADC. The digitized signal form is then digitally shaped with the trapezoidal method and the pulse height is extracted. A rise time of 2.4 μs and a flattop width of 0.8 μs were set to generate equivalent pulse shaping to the CAS. The pulse pile-up rejection was always

activated in the digital system. Gammavision was also used to set the shaping parameters and collect the pulse height spectrum.

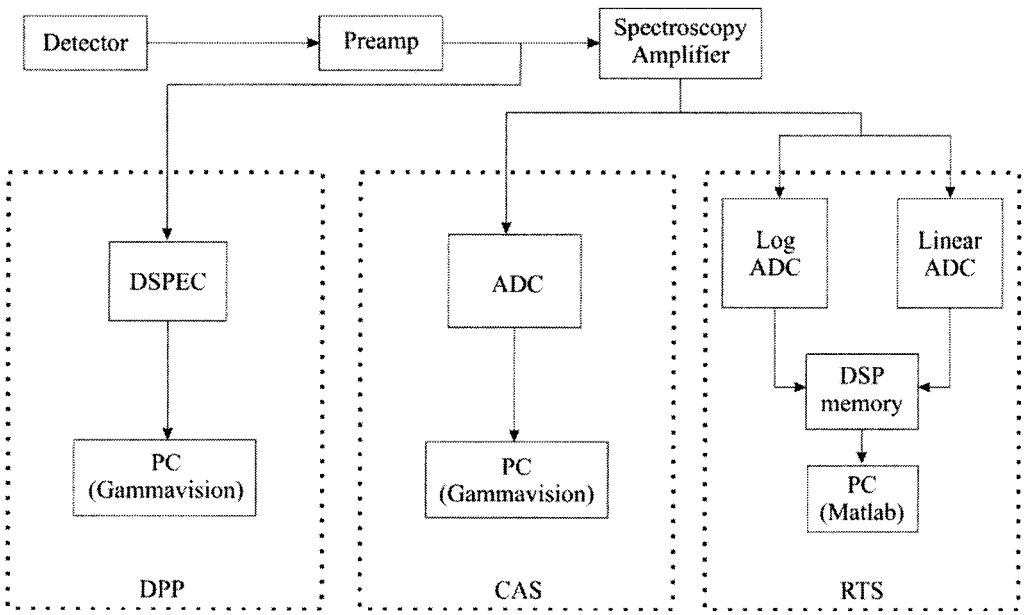

Figure 3.1: Schematic diagram of the pulse processing electronics setup for the three systems, DPP, CAS and RTS. Preamp: Preamplifier, ADC: Analog-to-Digital Converter, DSP: Digital Signal Processor, DSPEC: commercial digital pulse processing unit, PC: Personal Computer.

The RTS involves both a logarithmic ADC (NS-621 8192 ADC, Northern) and a linear ADC (FAST ADC 8077, Canberra). After pulse shaping using the same amplifier as the CAS, the signal is split and sent to the logarithmic and the linear ADCs. For each event, the bin address is given by the logarithmic ADC and the linear ADC address value, which is proportional to the absorbed energy, is added as the increment. The data are then stored in the DSP memory and the microdosimetry spectrum is displayed in real time using MATLAB software. A detailed description of the RTS was reported by Byun *et al.* (2007b).

The gain of each system was set to reach an upper level discriminator of ~ 200 keV/μm. The lower level discriminator (LLD) was set at ~ 1 keV/μm, right above the noise level. The linearity of each system was carefully calibrated with a high precision digital pulser (Model PB-5, Berkeley Nucleonics). In order to test the three systems comprehensively under various count rates and dose rates, both incident proton energy and current were widely varied. The proton energy was set at 1.8, 2.0, 2.1, 2.3 and 2.5 MeV and three different proton currents of, 100, 200 and 300 μA were delivered at each proton energy.

3.5 Calibration of Microdosimetric Spectrum

The raw data collected by the CAS and DPP generate a pulse-height spectrum. Each bin (channel number) is assigned a pulse height and the number of events is stored in the corresponding bin. As a result a spectrum with the number of counts (events) as a function of channel number is displayed. The RTS generates a raw microdosimetric spectrum displaying in real time the linear ADC channel number multiplied by the corresponding counts as a function of the logarithmic ADC channel number. In all three pulse processing systems the data are calibrated using the pulser to convert the channel number to pulse amplitude. Given a known lineal energy source, such as the internal alpha source of the spherical TEPC, the pulse amplitude can be converted to lineal energy. Figure 3.2 displays the raw alpha spectrum generated by the internal ^{244}Cm source of the

spherical TEPC as observed by RTS. As described in Section 2.2, the peak lineal energy of the internal ^{244}Cm alpha source is 127 keV/μm for a tissue simulated 2 μm diameter sphere. Using the peak lineal energy of the alpha source and the corresponding logarithmic ADC channel number the spectrum can be calibrated. A detailed explanation of the calibration steps is presented in the Appendix.

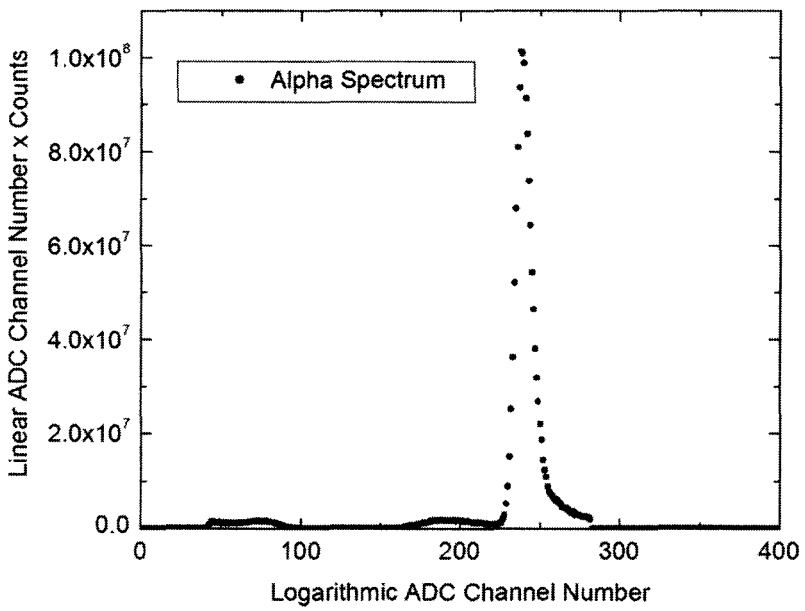

Figure 3.2: Spectrum obtained using the RTS of the internal alpha calibration source (^{244}Cm) in the spherical TEPC. This is the raw spectrum displaying logarithmic ADC channel number on the horizontal axis and linear ADC channel number multiplied by the corresponding counts on the vertical axis. The well known lineal energy of the ^{244}Cm alpha peak is used to calibrate the spectrum.

Once the data are calibrated the standard representation of the microdosimetric spectrum as presented in Figure 1.1 can be generated. The

absorbed dose, D in Gy is related to the area under the spectrum and can be calculated using:

$$D = 1.602 \times 10^{-16} \frac{\bar{l}}{\rho V} \sum_i y_i N(y_i) \tag{3.1}$$

where y_i is the lineal energy of each bin and $N(y_i)$ is the number of events detected with lineal energy y_i and $\bar{l}$ is the mean chord length. The summation in equation (3.1) includes all lineal energy bins and represents the area under the curve in the calibrated spectrum. The constant 1.602×10^{-16} is the conversion factor from keV to J, ρ is the density of the gas and V is the sensitive volume of the detector. Substituting the chord length for a 2 μm diameter sphere (equation (1.3)), the density of the gas, ρ_g and the volume, V of the spherical TEPC cavity described in Section 2.2 into equation (3.1) the dose measured with the spherical TEPC is calculated using:

$$D = 1.2646 \times 10^{-6} \sum_i y_i N(y_i) \qquad \text{[mGy]} \tag{3.2}$$

The dose rate, $\dot{D}$ can be obtained by dividing the dose D by the live time, t_{live} associated with the detection system. (The detection system refers to the detector and associated pulse processing components.)

$$\dot{D} = \frac{D}{t_{live}} \tag{3.3}$$

Equations (3.2) and (3.3) were used to calculate the dose rate of the measurements conducted with the spherical TEPC and the three pulse processing systems and are presented in the next section.

3.6 Results

The three pulse processing systems were compared in terms of performance in pulse height analysis, and consistency in dose spectrum and dose rate.

As a fundamental performance in pulse height analysis, the observed true-time count rate (throughput), i.e. the total number of counts divided by the real time, of each system was compared. All counts in the pulse height spectrum above 2.63 keV/μm were integrated to obtain the total counts. Figure 3.3 shows the observed true-time count rate as a function of the proton current measured by the DPP and CAS. The RTS throughput is not included in the figure because it accumulates the dose spectrum instead of the event pulse height spectrum. At 100 μA, there is little difference in throughput rate for all proton energies while the DPP shows a slight increase in throughput as the proton current increases. The maximum difference in throughput rate is 7 % at 2.5 MeV and 300 μA.

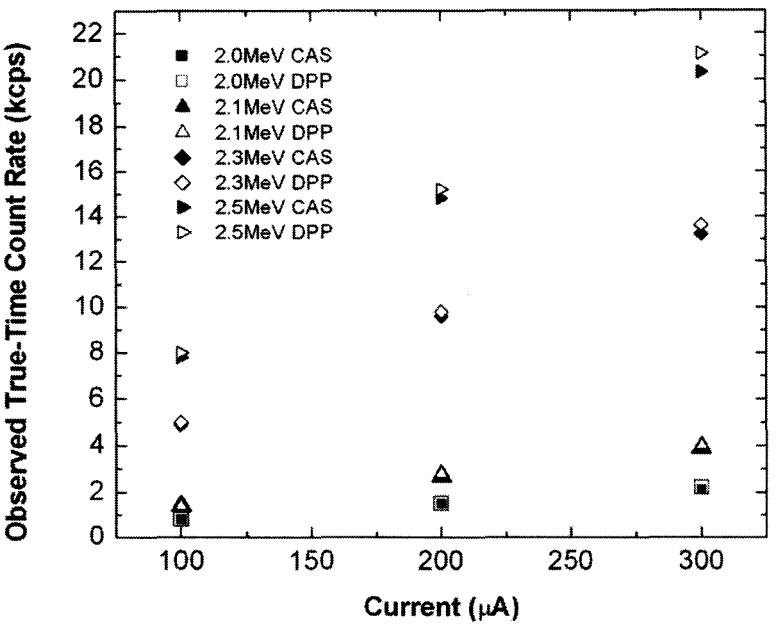

Figure 3.3: Comparison of throughput count rates for CAS and DPP. Throughput count rate is defined as the number of counts divided by the real time and is presented as a function of proton current. The error associated with the data is smaller than the symbol size. (Error is obtained by taking the square root of the counts and dividing by the real time.)

Another important parameter in pulse processing performance is the dead time. Figure 3.4 shows the dead time of each system as a function of proton current and energy. In analog pulse processing, the dead time for a detected event is the sum of the rise and fall times of the shaped pulse when the analog-to-digital conversion time is shorter than the fall time. The dead time is extended if the conversion is longer. Similarly, in digital processing, the dead time for a shaped pulse is the sum of the rise, fall and flat top times. The dead time pattern is comparable to the paralyzable model. To correct for the dead time, both CAS and DPP have internal live time clocks, which are turned off during the dead period

for each detected event following the above principle. The live time clock of the RTS was implemented in the same way. When a spectral collection is completed, true, live and percent dead times are reported.

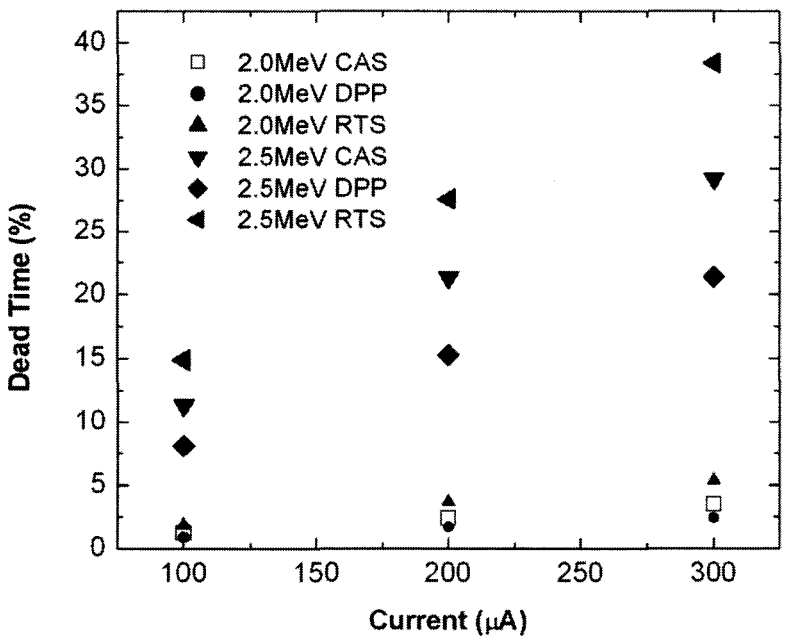

Figure 3.4: Comparison of dead times for CAS, DPP and RTS as a function of proton current at 2.0 and 2.5 MeV proton energies.

From the figure, for a fixed proton current, the neutron and gamma-ray fluence rates increase with increasing proton energy due to their yield dependence on proton energy. The corresponding increases in TEPC event rate at higher proton energies led to an increase in dead time. The dead time of the DPP is lowest among the three systems, which is consistent with the throughput performance in Figure 3.3. The RTS dead time was always highest, which

originates from the relatively low frequency (50 MHz) of the logarithmic ADC employed in the RTS. Of the three systems, the DPP showed the best performance in pulse processing speed.

In order to check the consistency in the dose spectral pattern, the microdosimetric spectra from the three systems were compared next. Figure 3.5 displays the microdosimetric spectra of the three systems obtained with proton energy of 2.0 MeV and current of 200 μA. A microdosimetric spectrum displays the lineal energy (y) on the horizontal axis with an equal logarithmic bin structure and the number of counts (N) multiplied by the corresponding lineal energy, yN(y), on the vertical axis. For a graphical comparison the RTS spectrum was multiplied by a factor of 2.2 since it contains ~130 bins in a decade for most of the lineal energy region while the measured spectra from the other two systems were redistributed with 60 bins per decade (Gerdung *et al.*, 1995).

From Figure 3.5, it is obvious that the patterns of the microdosimetric spectra are consistent with each other. The gamma-ray dose spectrum of the RTS below 10 keV/μm shows a noticeable deviation from the other two spectra since the logarithmic ADC has a significant nonlinearity in this low lineal energy region (Byun *et al.*, 2007b) and the number of bins per decade becomes much smaller as the lineal energy decreases. In other words, multiplying by a factor of 2.2 is not valid in this region. However, the quantitative gamma-ray dose value from the

RTS is still effective. (The multiplication factor was not incorporated in the dose calculations.)

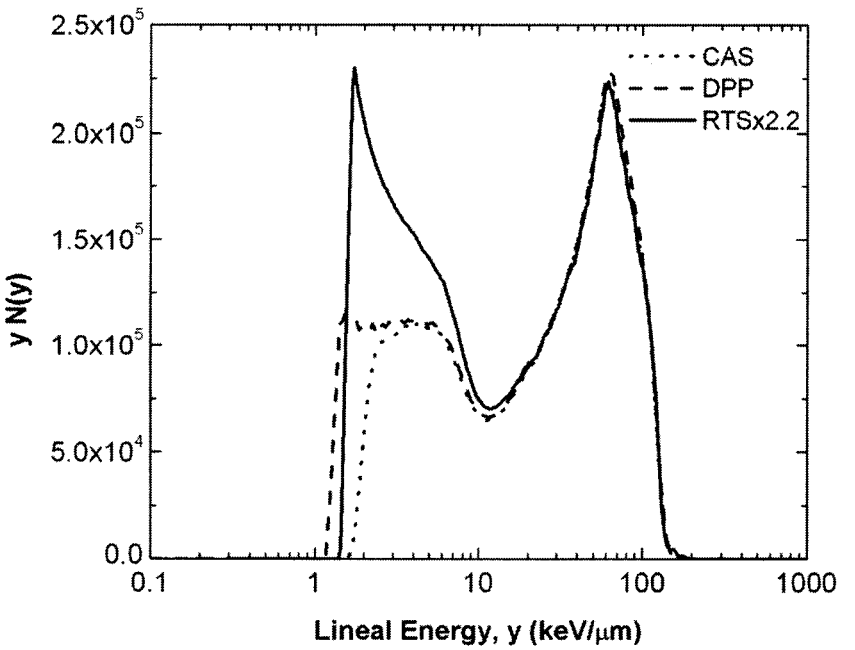

Figure 3.5: Comparison of Microdosimetric spectra for the three different systems, CAS, DPP and RTS. The proton energy and current were 2.0 MeV and 200μA, respectively.

Figure 3.6 shows the dose spectra after separation of the neutron and gamma-ray components. The separation was done by subtracting the gamma-ray component using the pure gamma-ray microdosimetric spectrum of each system, which was obtained below the ^{7}Li(p,n) threshold at the proton energy of 1.8 MeV. For convenience, part of the gamma-ray spectrum with small fluctuations near the LLD level was removed. As a result the lineal energy cut off was set at 4.24, 4.64 and 5.01 keV/μm for the RTS, DPP and CAS, respectively. The neutron or

gamma-ray dose was determined by integrating the corresponding component dose spectrum. In the case of the gamma-ray dose, the dose spectrum extends further down to the lineal energy of ~ 0.05 keV/μm and the integration was extrapolated using the standard full microdosimetric spectrum for ^{137}Cs, which is displayed in Figure 3.6.

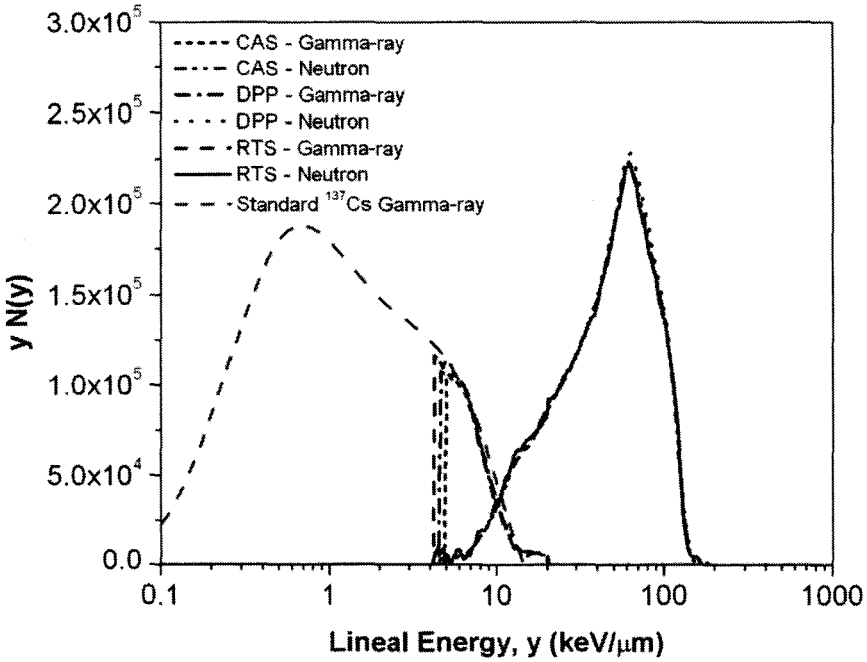

Figure 3.6: Neutron and gamma-ray dose spectra after separation. The standard gamma-ray Microdosimetric spectrum for ^{137}Cs is shown as well.

Figure 3.7 shows the neutron dose rate of each processing system as a function of the proton current. The neutron dose rate was obtained by dividing the neutron dose by the live time. The error bars in the figure represent 10% uncertainty, which is generally accepted for dose values obtained from

microdosimetric spectra (ICRU, 1983). This is a conservative estimation that takes into account the uncertainties due to the gas pressure, internal alpha source positioning, lineal energy calibration, etc. (ICRU, 1983). The statistical uncertainty was negligible in all cases. The lines in the figure represent simple linear fitting of three data points. For the DPP, each data set shows good linearity with respect to the proton current. The zero of each line corresponds to 0 mGy/min, which is consistent with the theoretical expectation of the dependence of neutron dose rate on proton current. However, the linear fit of 2.5 MeV data for the RTS has a significant positive intercept, which indicates an underestimation of the 300 μA data point when the fit is forced to have a zero intercept. An opposite bias is observed for the 2.5 MeV linear fit of the CAS.

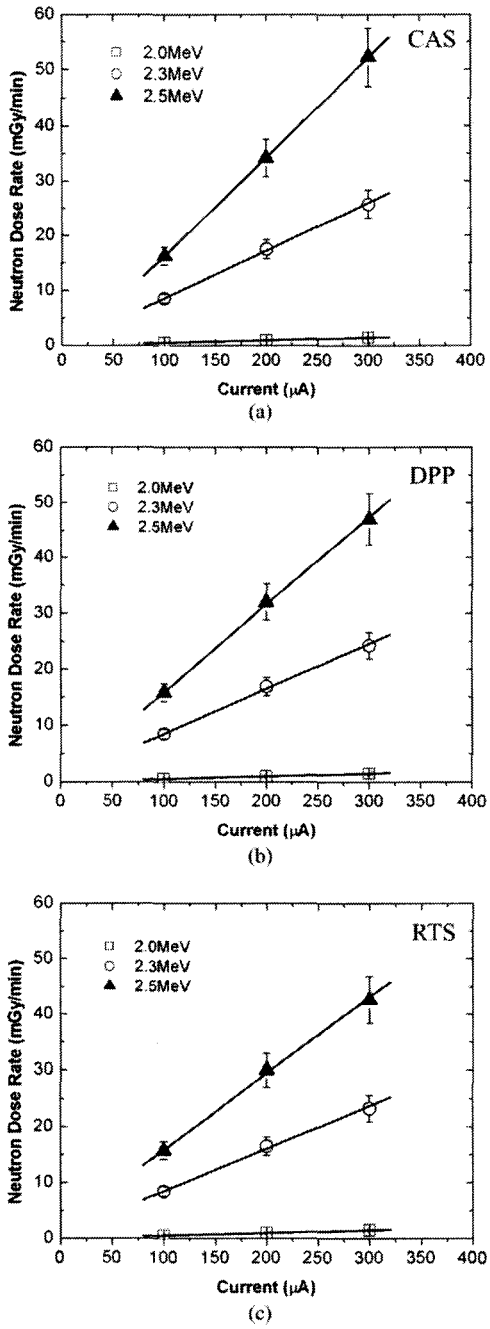

Figure 3.7: Neutron dose rate as a function of proton current for the different pulse processing systems: (a) CAS, (b) DPP and (c) RTS.

In Figure 3.8 the dependence of the neutron dose rate on the proton energy is compared at a fixed current of 200 μA. The neutron dose rates from the three systems are consistent with each other. The discrepancy in neutron dose rate between the three systems increases as the proton energy increases with the highest range of 12 % at 2.5 MeV.

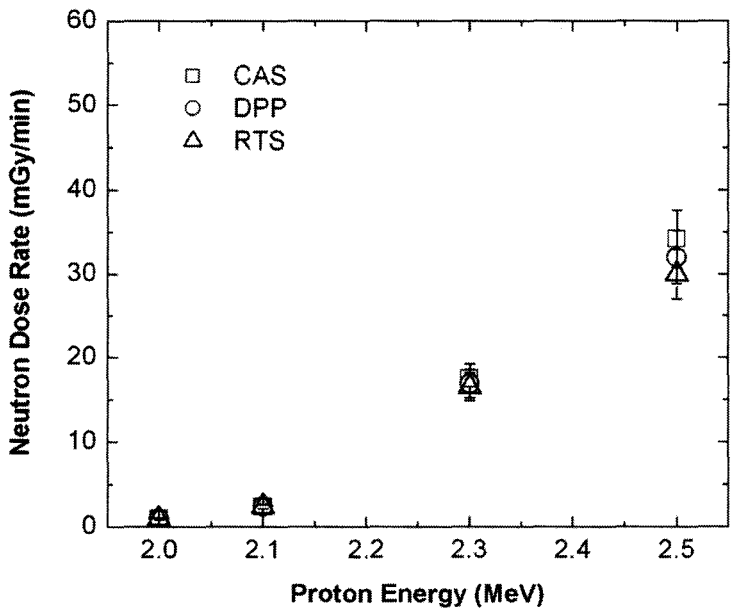

Figure 3.8: Comparison of neutron dose rates as a function of proton energy. The proton current was fixed at 200 μA.

In order to take a closer look at the discrepancy in neutron dose rate at 2.5 MeV, a bar graph of the neutron dose rate as a function of proton current is shown in Figure 3.9. At 100 μA, the neutron dose rates from the three systems are in excellent agreement within 2.7 % and any system can be employed reliably.

When the current was doubled, the DPP dose rate became twice the 100 μA dose rate while both RTS and CAS data show deviations from the corresponding values by 5 %. At 300 μA, the DPP data is still in good agreement with three times the value obtained at 100 μA within 1 % while the deviations of the RTS and the CAS reach 10 % and 7.4 %, respectively. Considering the higher dead times observed for the RTS and the CAS at 2.5 MeV, 300 μA in Figure 3.4, imperfect dead time corrections might have caused the systematic biases in neutron dose rate. From these measurements an extrapolation of the observed data to higher proton energies and current would lead to a continuing divergence in the neutron dose rate measured by the three systems. Supposing there was no change in the lithium target condition during measurements so that the neutron yield increased in proportion to proton current, although this must be confirmed by another neutron monitor with a moderate count rate, the DPP neutron dose rates are within the expected trend and therefore, the DPP may provide the best estimate of the true dose rate at high count rates. The observed lower system dead time and the pile-up rejection also support a preference for the DPP at high dose rates.

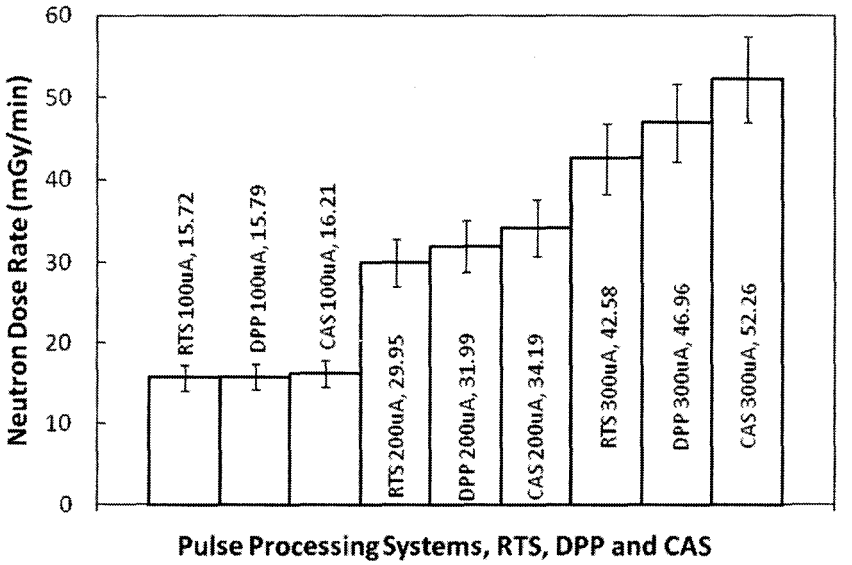

Figure 3.9: Comparison of neutron dose rates at proton energy of 2.5 MeV.

Along with consistent neutron dose rates obtained between all three systems at neutron dose rates lower than 30 mGy/min, the same trend was observed with the gamma-ray dose rate. Figure 3.10 displays the gamma-ray dose rate as a function of the proton current obtained by all three systems at the proton energy of 2.0 MeV. The percent difference in gamma-ray dose rate was less than 3 % between the three systems. At 2.3 and 2.5 MeV, the separation of the two dose components is not as obvious as at the proton energies closer to the ^{7}Li(p,n) threshold due to the limited portion of the gamma-ray spectrum available. Therefore, an increase in discrepancy between the three systems of the gamma-ray dose rates was found at these proton energies.

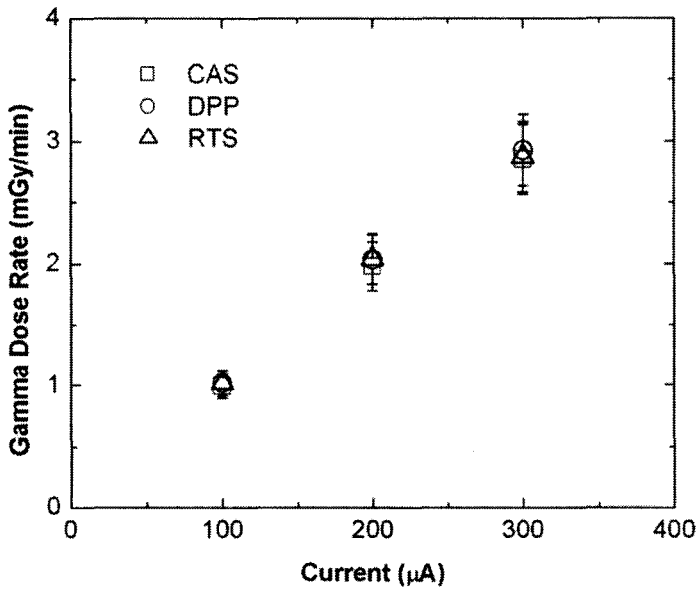

Figure 3.10: Gamma-ray dose rate as a function of proton current for the different pulse processing systems. The proton energy was set to 2.0 MeV.

3.7 Discussion

The three pulse processing systems for a TEPC detector were tested and compared for various neutron and gamma-ray dose rates using the McMaster Tandetron ^{7}Li(p,n) neutron source. In the fundamental aspects of the pulse height analysis, the DPP turned out to have the highest throughput and lowest dead time. At low and medium dose rates, all three systems were able to obtain consistent microdosimetric spectra and dose rates. At high dose rates, the CAS and the RTS showed noticeable deviations while the DPP kept good linearity with respect to the proton current at all proton energies investigated. Therefore, the DPP will be

more advantageous over the other two systems when a detector count rate is high and a fast pulse height analysis is the primary concern.

The RTS provides the microdosimetric spectrum conveniently in real time. However, its processing speed is much slower than those of the other two systems and therefore its operation in high dose rate is not desirable. The component with the slowest processing time in the RTS is the logarithmic ADC. By replacing the current 50 MHz clock in the logarithmic ADC with a faster one like 100 or 200 MHz, the processing speed can be greatly improved and may be comparable at least with the CAS processing speed.

Although the DPP is fast in processing, its dead time will eventually exceed 30 % as proton current increases further. In such a high dead time condition, the dead time correction must be a serious issue as identified for the other systems. Since there is little room to improve the pulse processing system, the sensitive volume of the TEPC detector must be reduced so that it can give a moderate count rate. To achieve this goal, a new type of the TEPC based on thick gas electron multiplier was developed and is under investigation (Byun *et al.*, 2009).

Chapter 4

Initial Experimental Tests with the THGEM TEPC: Signal Acquisition, Microdosimetric Spectrum, Measured Dose and Sensitive Volume Pressure Effects

4.1 Introduction

The goal of this investigation was (1) to obtain successfully a signal using the THGEM TEPC, (2) to compare the microdosimetric spectral pattern obtained with the THGEM detector with the standard TEPC, (3) to measure the dose with the THGEM TEPC and (4) to observe the effects of pressure change. These initial experiments conducted provided the first observations of the THGEM TEPC function and evidence of the potential capabilities of the detector. The results are presented in the following order: detector stability and reproducibility, gas multiplication, microdosimetric spectrum, measured dose and pressure effects. In these studies the detector contained a THGEM foil with an insulator thickness of (0.12 ± 0.02) mm and total thickness of (0.26 ± 0.02) mm (hereafter THGEM A). A proton beam energy of 2.3 MeV at a current of 150 μA was used to generate the mixed (n-γ) radiation field.

4.2 Materials and Methods

The THGEM TEPC was connected to the two pulse processing systems, RTS and CAS, as described in Chapter 3 and the detector is placed inside the irradiation cavity centred on the beam path. The irradiation cavity is described in Section 1.4. The detector was centred on the beam path and was placed in the irradiation cavity using the cavity opening at one of the sides of the cavity as shown in Figure 1.2. Figure 4.1 is a schematic diagram showing the connections of the experimental setup used to test the THGEM TEPC.

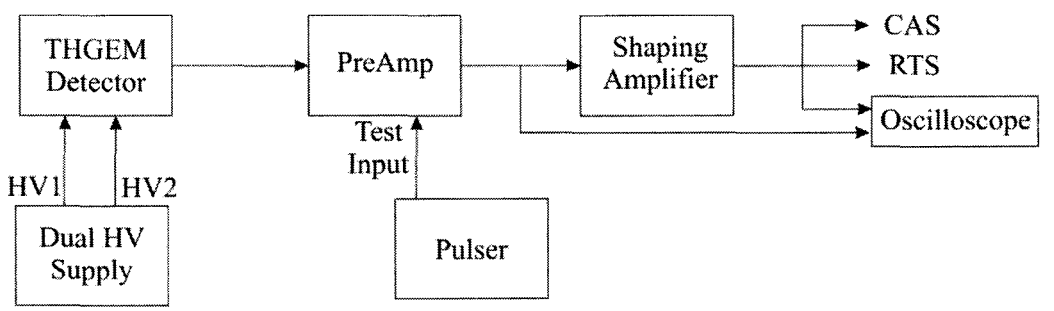

Figure 4.1: Experimental setup used to test the THGEM TEPC. The pulse generator (pulser) was used to test the preamp and for calibration purposes. The preamp and shaping amplifier outputs were connected to the oscilloscope to observe the generated signals prior to pulse processing. The adjustable voltage of the dual HV supply allowed the user to select the desired HV1 and HV2 values.

The two pulse processing systems were connected in parallel and used to collect the generated signals. In most of the post signal acquisition investigations the RTS data were analyzed, and the CAS was used to obtain the count rate and as the backup pulse processing system. The digital pulse generator (Model PB-5,

Berkeley Nucleonics) or pulser was used to test the function of the preamp and to calibrate the detected signals. The adjustable dual HV supply was used to provide the desired voltage to the drift cathode and the THGEM of the detector as described in Section 2.3.3. The resistor values of 10 MΩ and 1 MΩ were used for $R1$ and $R2$, respectively for all data obtained using THGEM A. The preamp and amplifier signals were continuously monitored using an oscilloscope (TDS 1012, Tektronix). Figure 4.2 displays the oscilloscope trace output signals from the preamplifier and shaping amplifier of the THGEM detector.

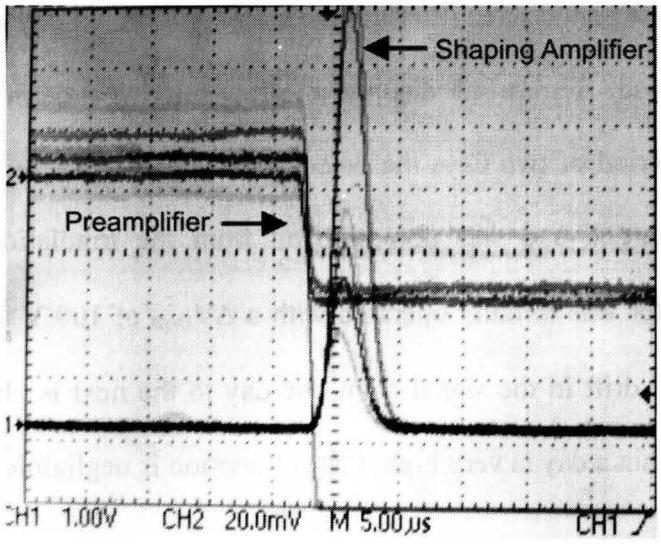

Figure 4.2: Preamplifier and shaping amplifier signals observed when the THGEM detector is exposed to the (n,γ) radiation field.

A wooden support was fabricated to centre the detector on the beam axis and to isolate electrically the detector aluminum casing from the surrounding graphite of the irradiation cavity. It was observed that contact of the aluminum

casing with the graphite within the irradiation cavity led to the grounding of the proton beam current via the THGEM detector. Once the experimental setup was complete, the mixed (n-γ) field was generated using a proton beam energy of 2.3 MeV and a current of 150 μA. The experimental setup described in this section was used for all data presented in this Chapter and Chapter 5.

4.3 Detector Stability and Reproducibility

The detector stability was observed by repeating the same experimental conditions over a period of time. Both the stability within a day and from day to day was observed. Figure 4.3 displays the raw microdosimetric spectrum over time. Over a period of two days the detector was centred on the beam path, ~ 8 cm from the target, and was not removed from the irradiation cavity. The THGEM detector was initially operated with a ΔV_{Drift} of 100 V and ΔV_{THGEM} of 636 V. A small drift in the signal from one day to the next is observed, but the consistency within a day is very high, that is variation is negligible.

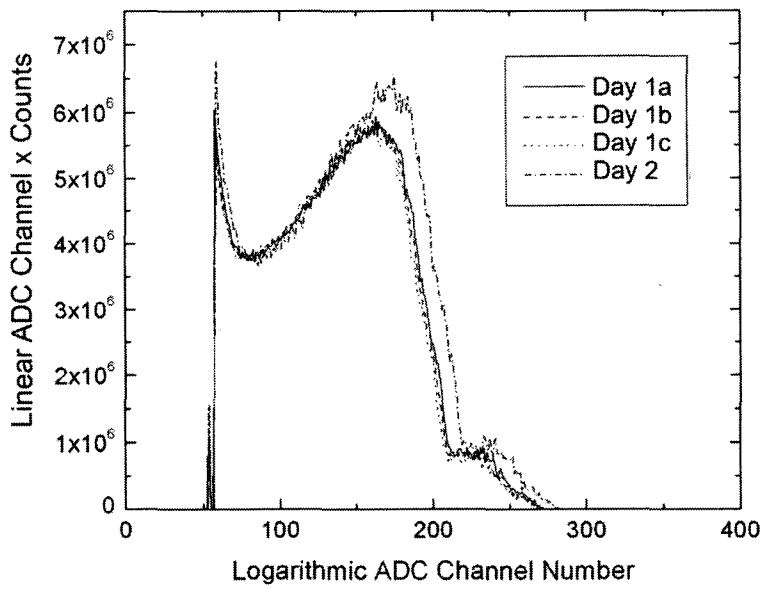

Figure 4.3: Microdosimetric spectra obtained using the RTS over a period of 2 days. Three spectra were acquired on the same day, Day 1a, 1b and 1c, and another, Day 2 acquired the next day using the same experimental setup.

High voltage power supply setting and pulse processing electronics (example amplifier gain) are all possible sources of signal drifts. As shown in Figure 4.3 these small drifts do not contribute to significant spectral shape changes. The spectra obtained within a day (Day 1a, 1b and 1c) are consistent while a very small drift toward increasing logarithmic ADC channel number is observed between the spectra obtained between Day 1 and Day 2. Note, due to the cumulative representation of the data on the vertical axis, a shift towards increasing logarithmic ADC channel number on the horizontal scale also leads to an increase in the vertical axis values. Although the day to day difference is

noticeable, the lineal energy calibration of the signal would account for signal drift, and the acquired data can thus be compared once calibrated.

The stability of the count rate detected by the THGEM TEPC over a time period of just over three hours was also observed. Each count rate measurement corresponds to a collection time of two minutes. Measurements were conducted at greater than two minute intervals. Figure 4.4 graphically displays the count rate measured as a function of time. A significant increase in the count rate measured was observed at 50, 56 and 69 minutes. These data points (squares) correspond to the time the proton beam was turned on after temporarily being turned off. This is an interesting observation possibly indicating the proton beam requires a short stabilization time once turned on. Thus the three square data points were excluded from the average count rate calculation of the THGEM stability. The solid line in Figure 4.4 represents the average count rate of all the relevant measurements with a value of 488 cps and a standard deviation of 4 cps. Overall, the count rate measurements are within 2% of the average. If the current was slightly unstable once the beam was turned back on it may have affected the measured count rate causing a larger than expected change to the count rate for the first 10 minutes, as depicted by the square data points in Figure 4.4. Overall, during the time measurements were conducted the count rate detected by the THGEM TEPC was within 2% of the average count rate. The stability and reproducibility of the THGEM TEPC with an insulator thickness of 0.12 mm and

total thickness of 0.26 mm was consistent and reliable. Data acquired with THGEM A within the detector were reproducible.

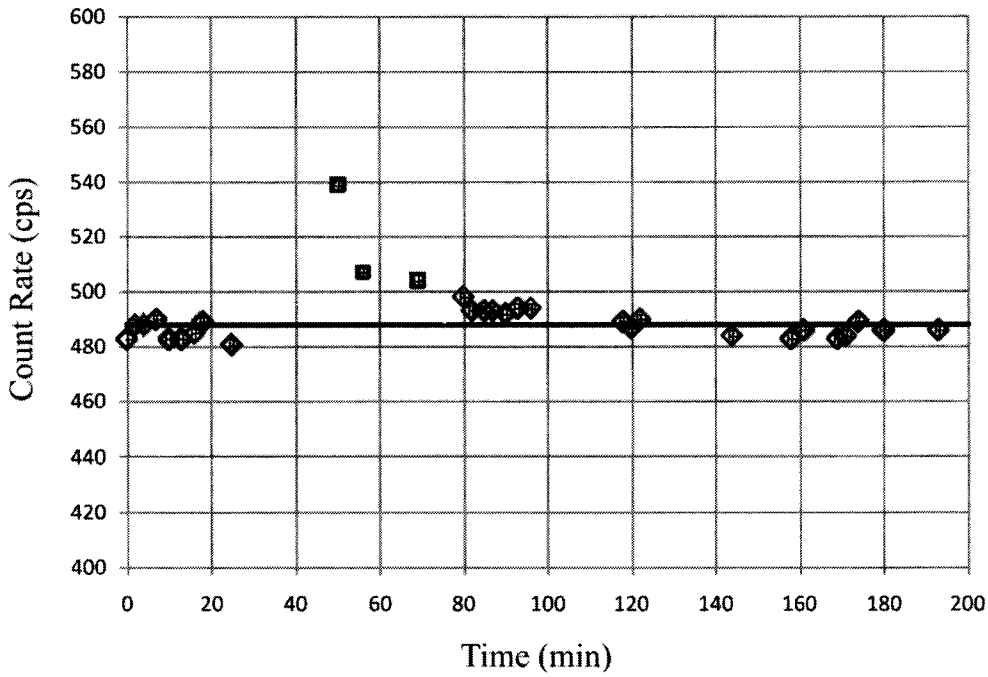

Figure 4.4: Systematic measurement of the count rate measured by the THGEM TEPC using a THGEM with insulator thickness of 0.12 mm. The CAS pulse processing system was used to acquire the gross count rate for a period of two minutes. Measurements were obtained at intervals of two minutes or greater. The solid line indicates the average count rate. A proton beam interruption occurred just prior the three square data points and as a result these points were not included in the average gross count rate.

4.4 Gas Multiplication

In order to assess the theoretical electron multiplication gain of the THGEM detector, the electric field profiles within the THGEM holes were numerically analyzed using Maxwell SV 2D software (Ansoft 2004) as described in Section 2.3.3. The data in Figure 2.5 display the electric field strength as a function of ΔV_{THGEM} as computed by the Maxwell 2D software. The electric field

along the axis of the holes linearly increases with increasing voltage across the THGEM as expected. Figure 4.5 (a) displays the raw experimental microdosimetric spectra obtained with the THGEM detector for varying voltage across the THGEM using the RTS pulse processing system. THGEM A with ID 3 (see Table 2.1) was used within the detector for the data presented in Figure 4.5. From this figure, the microdosimetric spectral pattern is clearly identifiable at all ΔV_{THGEM} values tested. Furthermore, as the voltage across the THGEM was increased, the neutron peak is shifted to the right due to the increase in electron multiplication with increasing THGEM voltage, and the gamma-ray dose component was also detected. The gamma-ray portion was obtained by decreasing the proton beam energy to 1.8 MeV, which is below the ^{7}Li(p,n) reaction threshold. In these proton beam conditions and using a ΔV_{THGEM} value of 745 V only the gamma-ray component was identified and is displayed in Figure 4.5 (a). The logarithmic ADC channel number corresponding to the neutron peak was used to quote the relative gain as a function of ΔV_{THGEM}. Figure 4.5 (b) displays the relative gain as a function of ΔV_{THGEM}. The vertical axis in Figure 4.5 (b) represents the logarithmic ADC channel number of the neutron peak centre at a given THGEM bias, ΔV_{THGEM}. The data were smoothed using adjacent averaging of 5 points prior to obtaining the neutron peak location. The maximum value of the neutron peak in Figure 4.5 (a) corresponds to the logarithmic ADC

channel number in Figure 4.5 (b). Thus an error of ± 5 channel numbers was assigned to the neutron peak location, and ± 9 V for the error in ΔV_{THGEM} associated with the HV2 dial setting. (The ΔV_{THGEM} is ± 9V for all relevant data presented.) As expected an exponential increase in relative multiplication gain is observed with increasing THGEM bias (note: the y-axis is a logarithmic scale).

Using THGEM A with ID 8 (see Table 2.1) the gain measurements were repeated using the same experimental conditions and the data were calibrated using the known lineal energy of the neutron peak. Similarly to Figure 4.5 (a), Figure 4.6 (a) displays the raw experimental microdosimetric spectra for varying voltage across the THGEM using the RTS pulse processing system. Figure 4.6 (b) displays the calibrated microdosimetric spectra and Figure 4.6 (c) is a graph of the relative gain as a function of ΔV_{THGEM}. Since this set of data was calibrated with lineal energy the relative gain is displayed as a function of the neutron peak amplitude in volts. The corresponding voltage of the neutron peak was obtained using a pulser, which is part of the spectrum calibration process used to convert to lineal energy. (Section 3.5 and the Appendix describe the calibration process.) As expected a logarithmic trend is observed. One of the visual advantages of calibrating the microdosimetric spectra is the ability to detect lower energy events with increasing ΔV_{THGEM}. As observed in the graph in Figure 4.6 (b), as ΔV_{THGEM} increases events with lower energy deposition are detected. The increase in gas multiplication of these lower energy events is above the electrical noise due to the

increase in ΔV_{THGEM}. Another interesting observation in Figure 4.6 (b) is the region of the spectrum at lineal energies greater than 150 keV/μm. There appears to be a small peak generated after the large neutron peak which is not present in the data displayed in Figure 4.5. This may be due to a possible non uniform gas multiplication effect within the THGEM holes which was not present in the THGEM A (ID 3) data presented in Figure 4.5.

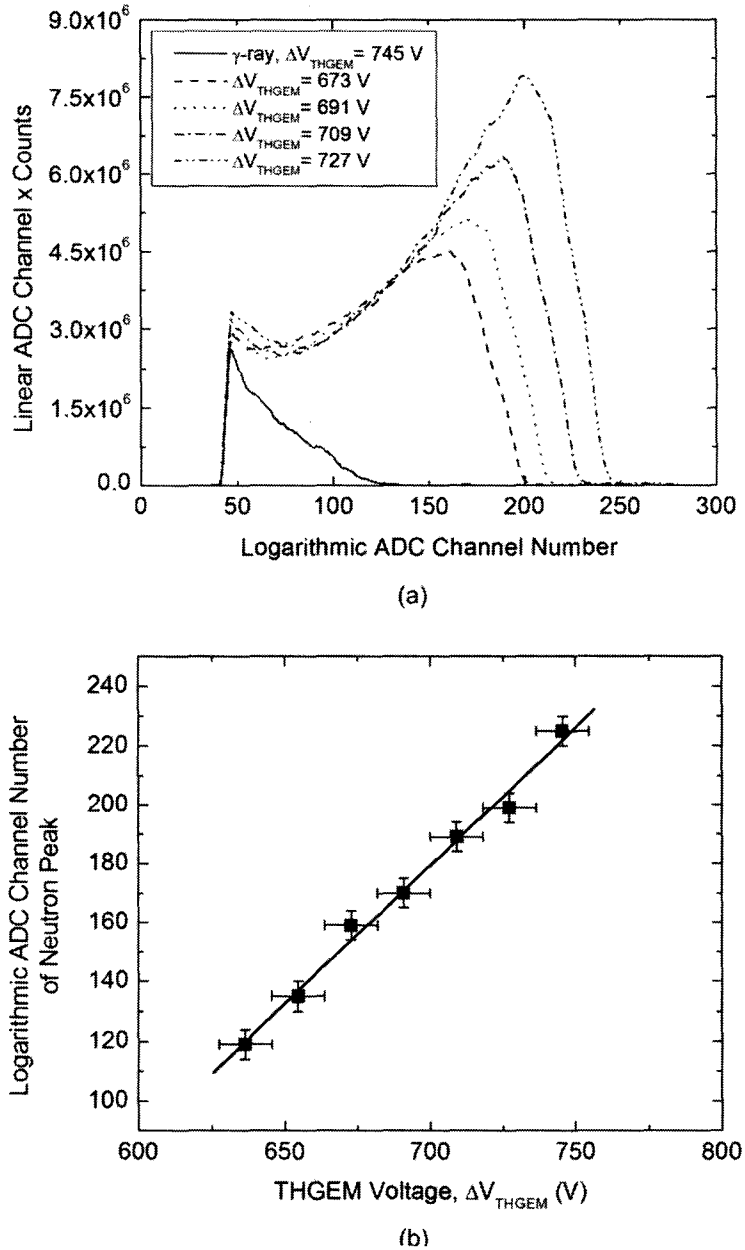

Figure 4.5: (a) The RTS spectra used to measure the relative gain, and (b) the relative gain as a function of ΔV_{THGEM} using a THGEM insulator thickness of 0.12 mm (ID 3). The gamma ray spectrum in (a) was obtained with a ΔV_{THGEM} value of 745 V. The relative multiplication gain in (b) was determined from the logarithmic neutron peak centre in (a).

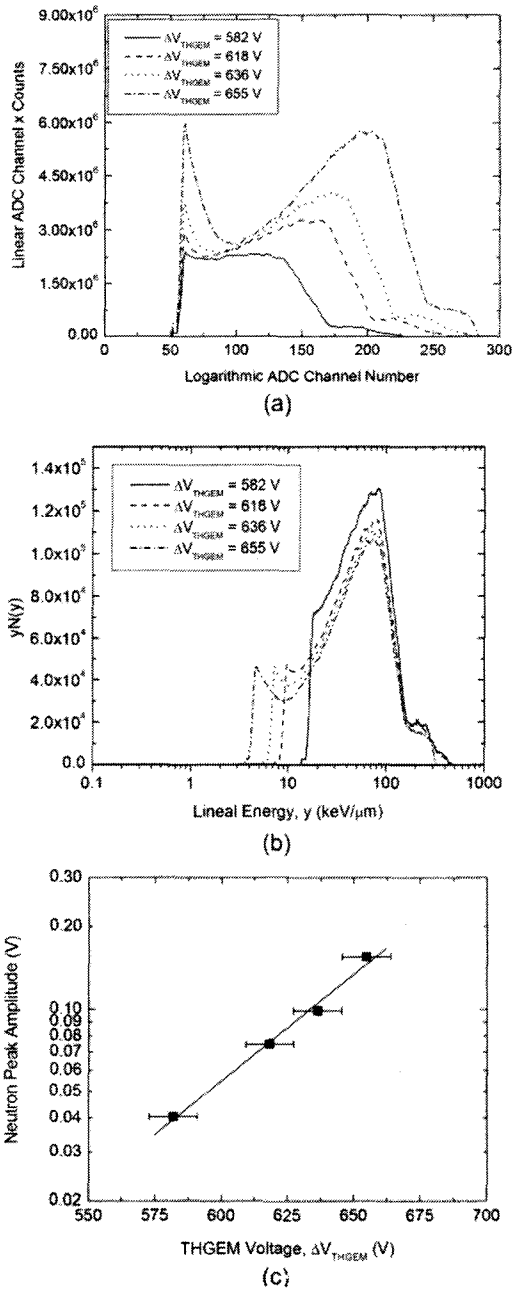

Figure 4.6: (a) Raw microdosimetric spectra obtained with THGEM A (0.12 mm insulator thickness, ID 8) using the RTS pulse processing system. (b) The calibrated microdosimetric spectra used to obtain the relative gain, and (c) the relative gain as a function of ΔV_{THGEM}. The relative multiplication gain in (c) was determined from the corresponding pulser signal amplitude of the peak location in (b). The errors associated with the Neutron Peak Amplitude are smaller than the data points.

4.5 Microdosimetric Spectrum

Figure 4.7 presents the microdosimetric spectra obtained with a standard 0.5 inch spherical TEPC (LET-1/2, Far West Technology, Inc.) and with the THGEM detector. Figure 4.7 (a) displays the experimental data obtained February of 2008 while Figure 4.7 (b) displays the experimental data obtained September of 2009. Both data sets were obtained with the same experimental conditions with the same thickness THGEM, but a different THGEM was used in each data set collected. The data are displayed with the lineal energy, y in keV/μm on a logarithmic scale on the horizontal axis and the corresponding number of events multiplied by the lineal energy, yN(y) on the vertical axis. The calibration of the lineal energy was carried out by using the internal alpha source of the spherical TEPC. The internal alpha source is ^{244}Cm and has a known lineal energy of 127 keV/μm (in TE gas for a 2 μm diameter) and is used to convert the pulse height to lineal energy as explained in Section 3.5. Since the spectra shown in Figure 4.7 were obtained at the same proton energy of 2.3 MeV, the lineal energy of the neutron peak is the same for both detectors. Thus, once the spectrum obtained with the spherical TEPC is calibrated, the neutron peak lineal energy can be used to calibrate the spectrum obtained with the THGEM detector. The THGEM TEPC detector voltage settings used were: ΔV_{Drift} = 180 V and ΔV_{THGEM} = 745 V for the data presented in Figure 4.7 (a) and ΔV_{Drift} = 160 V and ΔV_{THGEM} = 582 V for the data in Figure 4.7 (b). For a qualitative comparison the spectra

obtained with the THGEM detector are also scaled to the spherical TEPC spectra. An interesting observation from the data in Figure 4.7 is the minimum lineal energy detected by the THGEM detector between the two data sets and the different ΔV_{THGEM} values used on the two occasions. Although different ΔV_{THGEM} values were used, Figure 4.7 (a) which corresponds to the data obtained with the higher ΔV_{THGEM} value compared to Figure 4.7 (b) is able to detect lower energy events as expected. Furthermore, from Figure 4.7, it is obvious that the spectrum obtained with the THGEM detector is comparable to the standard spherical TEPC spectrum. This is a promising result on the development of a new, cost-effective and easy to manufacture TEPC based on the THGEM.

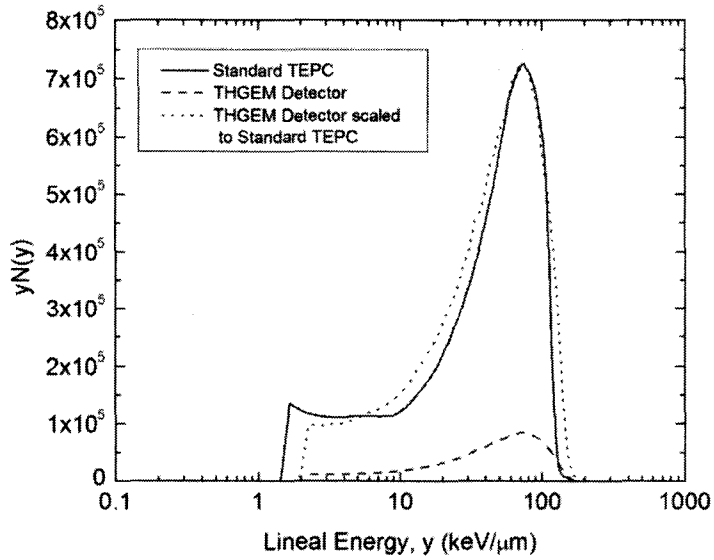

Figure 4.7: Comparison of measured microdosimetric spectra between the THGEM detector and the standard TEPC collected at E_p = 2.3 MeV. In order to compare the shape of the spectrum the THGEM spectrum is normalized to the standard TEPC spectrum (dotted curve). Data in (a) were obtained in February of 2008 using THGEM A, ID 3 and data in (b) obtained in September of 2009 with THGEM A, ID 8.

4.6 Absorbed Dose Measured with the THGEM TEPC

Once the data are calibrated, the absorbed dose measured with the THGEM detector can be calculated and compared to the dose measured with the standard TEPC. Using the calibrated spectra presented in Figure 4.6 (b) the dose rate for the four different ΔV_{THGEM} values used can be calculated. The dose rate was obtained using the equation (3.1) and (3.2) described in Section 3.5. Starting with equation (3.1) and substituting 2 μm for the diameter of the simulated tissue volume for the chord length equation (1.4), equation (3.1) is simplified to:

$$D = 1.602\times10^{-16}\left(\frac{2\times2\mu m}{3}\right)\frac{1}{\rho V}\sum_i y_i N(y_i) \quad [Gy] \tag{4.1}$$

where ρV in equation (4.1) is the mass of the TE gas within the sensitive volume (SV) and can be calculated using the following steps:

$$\begin{aligned}
\rho V &= \rho_g \pi r^2 h \\
&= (\rho_g r_g)\pi 2r^2 && \text{(Since SV is a right cylinder, } h = 2r\text{)} \\
&= (\rho_t r_t)\pi 2r^2 && \text{(Using the relation defined by equation (2.3))} \\
&= ((1g/cm^3)(1\mu m))\pi 2(0.25)^2 && \text{(Simulating a } 2\mu\text{m diameter right cylinder)} \\
&= 3.927\times10^{-5} g = 3.927\times10^{-8} kg
\end{aligned}$$

Substituting the numerical value of 3.927×10^{-8} kg for ρV in equation (4.1) the dose measured by the THGEM detector can be calculated using:

$$D = \frac{1.602\times10^{-16}}{3.927\times10^{-8}kg}\left(\frac{2\times2\mu m}{3}\right)\sum_i y_i N(y_i) \quad [Gy]$$
$$= 5.439\times10^{-9}\sum_i y_i N(y_i) \quad [Gy] \qquad (4.2)$$
$$= 5.439\times10^{-6}\sum_i y_i N(y_i) \quad [mGy]$$

Once the area under the microdosimetric spectrum is obtained the dose can be calculated using equation (4.2). Finally, the dose rate is obtained by dividing equation (4.2) by the live time of the system. Table 4.1 displays the required data to obtain the dose rate using equation (4.2):

Table 4.1: Dose rate obtained with THGEM detector using the area defined by the microdosimetric spectra shown in Figure 4.6 (a).

ΔV_{THGEM} (V)	Area (keV/μm)	Dose* (mGy)	Live Time (min)	Dose Rate** (mGy/min at 150μA)
582 ± 9	1.15×10^7	62.55	10	6.3 ± 0.6
618 ± 9	1.18×10^7	64.10	10	6.4 ± 0.6
636 ± 9	1.19×10^7	64.91	10	6.5 ± 0.6
655± 9	1.21×10^7	65.70	10	6.6 ± 0.7

*Dose obtained using equation (4.2)
**Dose rate obtained by dividing Dose values by the Live Time. A 10% error is associated with the dose rate.

The dose rates listed in Table 4.1 are also depicted graphically in Figure 4.8. The dashed line represents the mean of the dose rate obtained with the THGEM detector. The mean value is 6.4 with a standard deviation of 0.1 mGy/min per 150 μA. The solid line represents the dose rate measured by the standard TEPC. The dose rate measured with the standard TEPC under the same irradiation conditions was 8.7 ± 0.9 mGy/min per 150 μA. Between the two detectors a percentage difference of 26 % was observed in the measured dose rate.

Observing the data points in Figure 4.8, the dose rate appears to be slightly increasing with increasing ΔV_{THGEM} values.

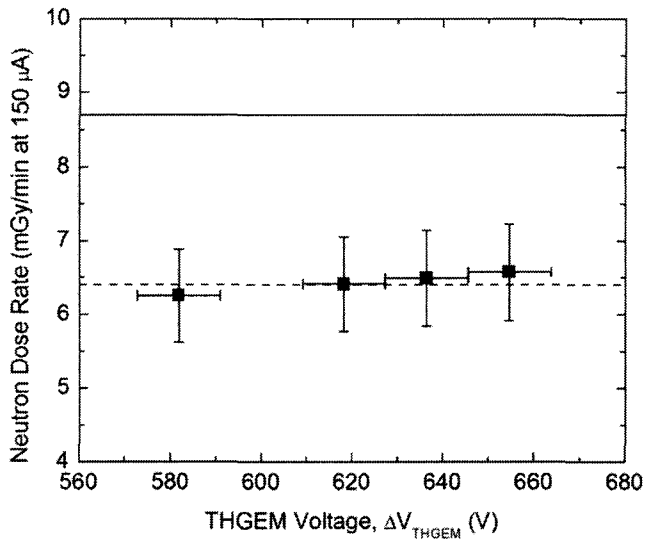

Figure 4.8: Measured neutron dose rate with the THGEM detector and standard TEPC. The data points correspond to the spectra shown in Figure 4.6(a). The dashed line is the mean of the dose rate measured with the THGEM detector and the solid line represents the dose rate measured with the standard TEPC. A constant dose rate is expected.

4.7 Pressure Effects

The final experiment conducted with THGEM A involved varying the pressure of the TE gas within the sensitive volume of the THGEM detector. The gas pressure within the sensitive volume is related to the volume of tissue being simulated. Furthermore, the pressure within the sensitive volume is related to the multiplication gain:

$$\ln M \propto \frac{E}{P_g} \tag{4.1}$$

where M is the multiplication gain, E is the electric field within the THGEM holes and P_g is the gas pressure. A detailed explanation of the relationship between gain, electric field and pressure can be found in Kliauga *et al.* (1995). It was of interest to investigate how multiplication is affected when the pressure is varied. In the results presented so far in this chapter the pressure within the sensitive volume used was 167 torr which simulates a 2 μm diameter right cylindrical volume of tissue. The goal of this experiment was to observe how ΔV_{THGEM} is affected as a function of gas pressure. This was conducted by varying ΔV_{THGEM} for different pressure values until the gas multiplication was consistent with the multiplication observed at a gas pressure of 167 torr. The proton beam parameters were maintained at E_p = 2.3 MeV and I_p = 150 μA during all gas pressured tested. Table 4.2 lists the different TE gas pressures tested and the corresponding simulated diameter of the right cylindrical tissue volume.

Table 4.2: TE gas pressure used to simulate different size tissue volumes. The gas pressure was calculated using equations (1.8) and (2.4) as described in Chapter 2.

TE Gas Pressure (torr)	Sensitive Volume (mm^3)	Simulated Diameter (μm)	Simulated Volume (μm^3)
250 ± 5	98	3	21
167 ± 5	98	2	6
83 ± 5	98	1	0.8
42 ± 5	98	0.5	0.1

The experimental procedure involved identifying the neutron peak location and matching the same location to obtain the required ΔV_{THGEM} value at all the different gas pressures. For example, using the gas pressure of 167 torr,

the neutron peak location is noted as Channel Number X. Once the gas pressure within the detector is changed to the next value, the detector is again exposed to the same radiation field and the THGEM voltage is increased while observing the real time spectrum using the RTS pulse processing system. Once the neutron peak location reaches Channel Number X a spectrum is obtained and the value of ΔV_{THGEM} is noted. Figure 4.9 displays the spectrum obtained with gas pressures of 167, 83 and 42 torr. A collection time of 1200 seconds was used for each spectrum. Unfortunately, for the gas pressure of 250 torr breakdown of the detector was observed soon after the neutron peak location was matched to the reference channel number. As a result a complete spectrum was not obtained but the value of ΔV_{THGEM} was noted.

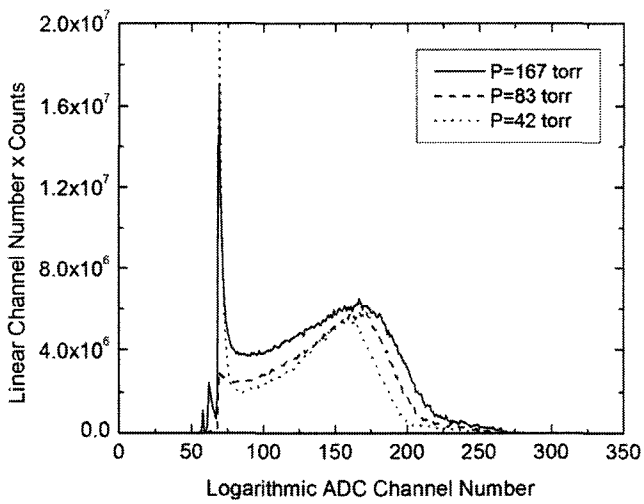

Figure 4.9: Microdosimetric spectra obtain with the RTS pulse processing system at varying TE gas pressure.

In Figure 4.10 the relationship between TE gas pressure and ΔV_{THGEM} required to observe the same multiplication gain is presented. The lower the gas pressure within the detector the smaller the tissue volume simulated as shown in Table 4.2.

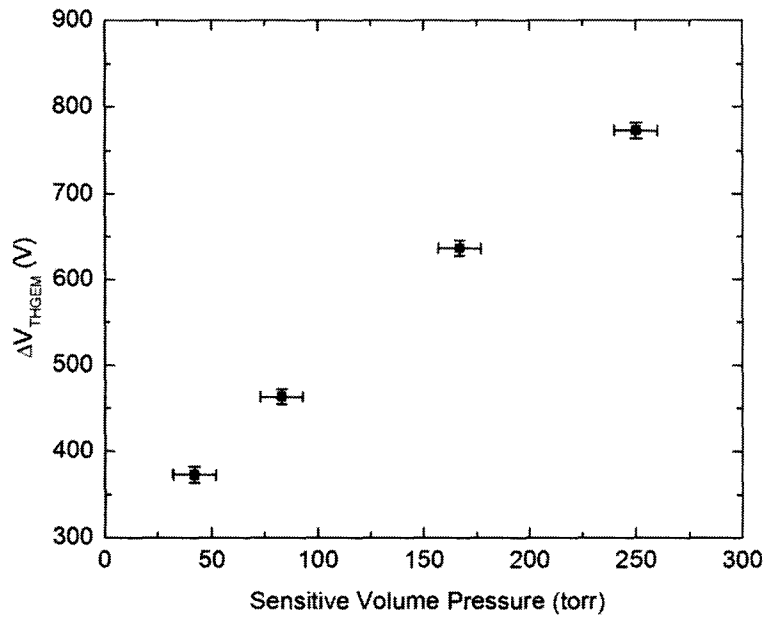

Figure 4.10: Relationship observed between the gas pressure within the sensitive volume of the detector and the voltage applied across the THGEM, ΔV_{THGEM}.

From the graph, the lower the gas pressure within the detector the lower the voltage across the THGEM is required to obtain the same multiplication gain, indicating the lower the gas pressure the higher the gain. For the gas pressure of 250 torr, a large voltage was required across the THGEM to obtain the same multiplication gain as observed at the lower pressures. Since a breakdown of the

detector was observed at the THGEM voltage of 772 V and gas pressure of 250 torr, the discharge threshold value of the THGEM for these conditions is near or at 772 V.

4.8 Discussion

The THGEM TEPC was assembled, and initial experiments conducted displayed expected results. The goal of the initial studies was to obtain a signal from the detector and to observe a microdosimetric spectrum using mixed-field radiation. The initial experiments provided the basic parameters required for the function of the detector and confidence on the stability of the THGEM detector. By varying ΔV_{THGEM} the relative increase in the multiplication gain was observed as shown in Figures 4.4 and 4.5. An exponential increase in gain as a function of ΔV_{THGEM} was observed as expected. Using a mixed-field radiation field, both gamma rays and neutrons were observed at the higher THGEM voltages. The onset of gamma-rays was observed around $\Delta V_{THGEM} = 590$ V across the THGEM. With increasing voltage across the THGEM lower energy gamma rays were observed. When the THGEM voltage was increased to values greater than $\Delta V_{THGEM} = 745$ V discharge events were observed causing a breakdown of the signal. For the THGEM thickness presented here a ΔV_{THGEM} of 727 V was sufficient to obtain the mixed-field microdosimetric spectrum. Although the

measured dose rate with the THGEM detector was lower than the standard TEPC measurement, the dose rate as a function of THGEM voltage was constant. This is a positive result indicating the THGEM detector is functioning as a proportional counter as expected. Further studies need to be conducted to understand the discrepancy in the measured dose rate. Finally, the effects of pressure in the sensitive volume of the THGEM detector provided additional information on the capabilities of the detector. The ability to observe microdosimetric spectra at different pressures allows for different tissue size simulations.

Overall the prototype detector generated expected signals and is comparable to the spherical TEPC results. Additional research will provide insight on the THGEM characteristics and improve the overall THGEM-TEPC performance.

Chapter 5

Observations of Increasing THGEM Insulator Thickness

5.1 Introduction

The motivation for the investigations presented here was to explore the possibility of increasing gas gain as a function the THGEM insulator thickness. Three additional THGEM insulator thicknesses were investigated: 0.40 mm, 0.70 mm and 1.48 mm. Unexpected results were obtained during these experiments but insights on the function of the THGEM detector were observed. The results for each THGEM insulator thickness tested include detector stability and reproducibility, gas multiplication and microdosimetric spectrum and measured dose rate. The same experimental setup described in Section 4.2 of Chapter 4 was also used to test the THGEMs presented in this Chapter. Two proton beam energies were used, 2.3 MeV and 2.1 MeV, both with a beam current of 150 μA.

5.2 Motivation for Increasing the THGEM Insulator Thickness

As described in Chapter 4, the results obtained using THGEM A (0.12 mm insulator thickness) were positive and have provided a foundation for the further development of the THGEM TEPC detector. Although THGEM A provided

positive results, simulations conducted with a larger insulator thickness indicated an increase in gas multiplication for the same electric field values applied within the THGEM holes (Byun *et al.*, 2009). Figure 5.1 is an illustration of two THGEM holes with different thickness, Δx_1 and Δx_2, and the resulting gas multiplication. Given the expected increase in gain with increasing THGEM insulator thickness observed with simulation studies, the goal of the work presented in this Chapter was to test THGEMs with varying insulator thickness and obtain an increased gain compared to THGEM A presented in Chapter 4.

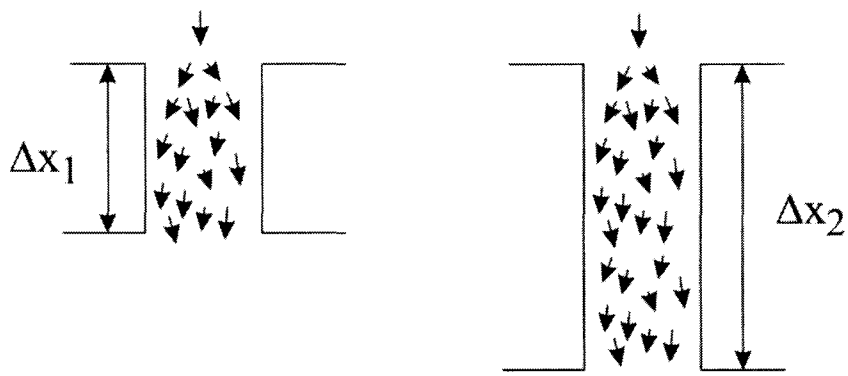

Figure 5.1: Increase in electron multiplication due to increased insulator thickness in THGEM. In this illustration the same electric field exists in both holes, but due to the increase in thickness, the available length for gas multiplication is longer in the hole with insulator thickness Δx_2 as compared to the hole with the shorter insulator length, Δx_1. The arrows within the holes represent electron multiplication.

5.3 THGEM B: Insulator Thickness 0.40 mm

THGEM B was fabricated with an insulator thickness of 0.40 mm and placed within the THGEM detector assembly. The diameter and pitch of the THGEM holes remained the same as in THGEM A. The values of R1 and R2 in

the detector were 10 MΩ and 0.87 MΩ, respectively. Several experiments were conducted to observe the function of THGEM B within the detector. The detector stability, gas multiplication, microdosimetric spectrum generated and measured dose rate with THGEM B will be presented and analyzed. The behaviour of THGEM B was not as stable as observed with THGEM A, but the overall performance of THGEM B is similar to the results of THGEM A presented in Chapter 4.

5.3.1 Detector Stability and Reproducibility

The detector stability of THGEM B was observed using two different proton beam energies. The first stability experiment was conducted using a proton energy of 2.1 MeV at 150 μA for the beam parameters and measured the gross count rate using the CAS pulse processing system for 5 minutes over a time period of 7 days. In these studies the operating voltages were slightly varied as breakdown was observed. ΔV_{Drift} was always set at 100V, while ΔV_{THGEM} was slowly decreased from 938 V to 902 V and finally to 883 V. In Figure 5.2 (a), day 1 data correspond to ΔV_{THGEM} = 938 V, day 2, 3, 4 and the first two data points of day 7 were obtained with ΔV_{THGEM} = 902 V, while the remainder of day 7 was obtained with ΔV_{THGEM} = 883 V. As shown in Figure 5.2 (a) the count rate detected with the THGEM detector is not stable. As a result a second stability test was conducted with beam parameters: 2.3 MeV proton energy and 150 μA

current. The detector operating voltages were: ΔV_{Drift} = 100 V and ΔV_{THGEM} = 883 V. Figure 5.2 (b) displays the count rate detected at these experimental parameters. The stability was observed over two consecutive days by measuring the gross count rate for two minutes using the CAS pulse processing system. From Figure 5.2 (b) the count rate measured by the detector with THGEM B is decreasing over time. The goal of increasing the proton energy was to observe if the beam parameters have an effect on the THGEM detector function. The results of this study are shown in Figure 5.2 (b). Similarly to Figure 5.2 (a) the count rate did not remain stable. One common observation in both measurements is the overall decrease of the count rate over time. Even in the few cases where a jump towards increasing count rate occurs, the rate begins to decrease quickly thereafter (see days 1, 2 and 4 in Figure 5.2 (a) and day 1 in Figure 5.2 (b)).

5.3.2 Gas Multiplication

Using THGEM B the electron multiplication gain as a function of ΔV_{THGEM} was measured. These measurements were obtained with beam parameters: 2.3 MeV proton energy at 150 μA, and the THGEM detector operating voltages were: ΔV_{Drift} = 100 V and ΔV_{THGEM} values used were 736 V, 773 V, 810 V, 846 V and 883 V. The measured spectra were calibrated using the known lineal energy of the neutron peak corresponding to the beam proton energy of 2.3 MeV.

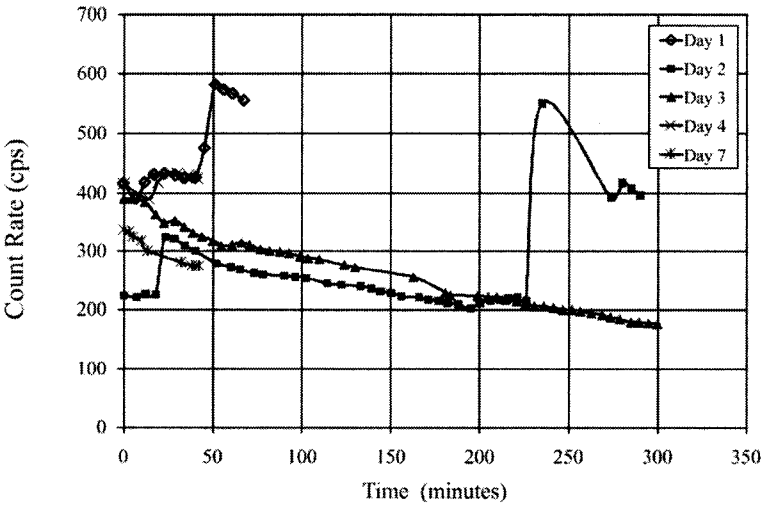

Figure 5.2: Systematic measurement of the count rate measured with THGEM B (0.40 mm insulator thickness). The CAS pulse processing system was used to obtain the gross count rate for a period of (a) five minutes and (b) two minutes. Measurements were obtained at intervals of two minutes or greater. Beam parameters: (a) 2.1 MeV proton energy, 150 μA current, (b) 2.3 MeV proton energy, 150 μA.

Figure 5.3 (a) displays the calibrated microdosimetric spectra obtained with THGEM B. An unexpected second small peak at the high lineal energies was detected with four out of the five THGEM voltages applied. The spectrum obtained with ΔV_{THGEM} of 810 V was the only spectrum without the second peak. As ΔV_{THGEM} is increased, the gain of the amplifier is adjusted to ensure all events are within the channel range specified by the software Gammavision. It was observed during data analysis that the gain used for this set of data was too high and thus data with higher pulse heights were not detected. As a result for the ΔV_{THGEM} of 810 V the second peak was above the specified channel range and is cut off from the displayed spectrum in Figure 5.3 (a).

Figure 5.3 (b) is a graph of the relative gain as a function of ΔV_{THGEM}. Similarly to Figure 4.6 (b), the relative gain is displayed as a function of the measured neutron peak amplitude in volts obtained before the conversion to lineal energy. An interesting observation in Figure 5.3 (b) is the trend of the relative gain. A linear trend on a logarithmic scale was expected as observed in Figures 4.4 (b) and 4.5 (b). The trend of the data displayed in Figure 5.3 (b) is clearly not linear indicating the detector THGEM voltages used are extending outside the proportional region of operation. This is an interesting observation and may be related to the voltage applied across the THGEM holes. It appears as though the low voltages displayed in Figure 5.3 (b) are below the proportional region threshold voltage.

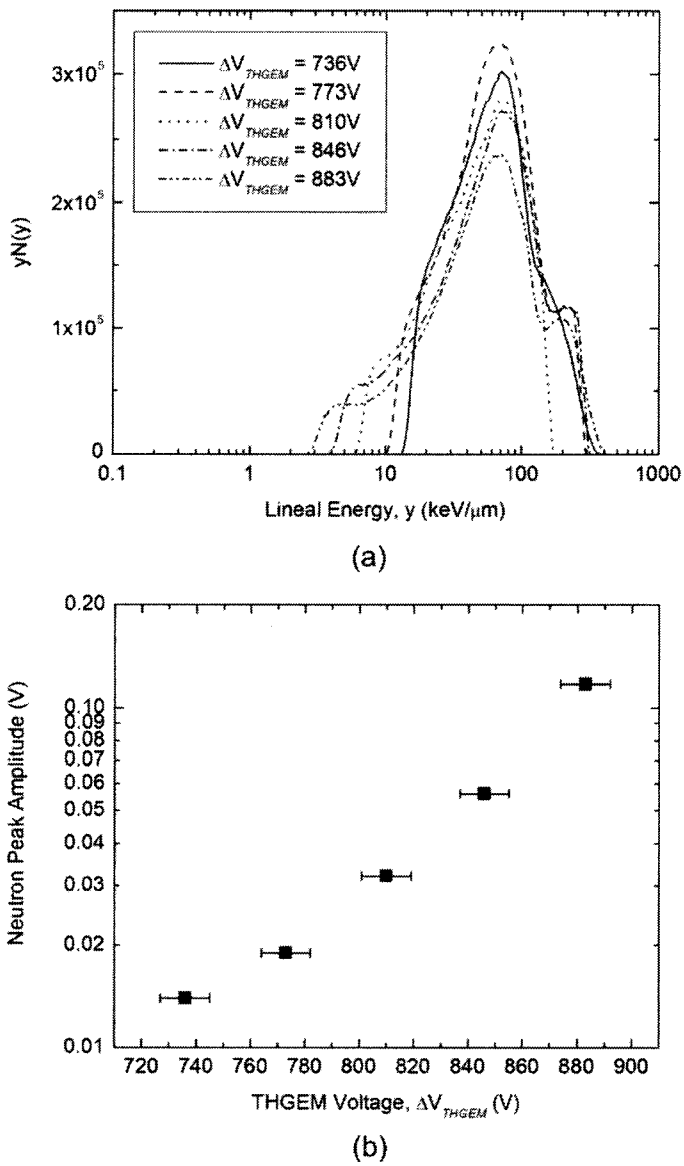

Figure 5.3: (a) The calibrated microdosimetric spectra used to measure the relative gain with THGEM B (0.40 mm insulator thickness) and (b) the relative gain as a function of ΔV_{THGEM}. The relative gain in (b) was determined from the corresponding signal amplitude of the peak location in (a). The errors associated with the Neutron Peak Amplitude are smaller than the data points.

5.3.3 Microdosimetric Spectrum

Two of the calibrated spectra measured with THGEM B presented in Figure 5.3 were used to compare the spectral shape of the microdosimetric spectrum obtained with the standard 0.5 inch spherical TEPC. Figure 5.4 displays the two spectra obtained with the THGEM detector and the standard TEPC spectrum obtained using the same beam parameters. The spectra obtained with ΔV_{THGEM} values of 810 V and 883 V are used to compare with the standard TEPC. These two curves were chosen to compare to the standard TEPC because of the different spectral shapes measured. The data obtained at $\Delta V_{THGEM} = 810$ V compares well with the standard TEPC and has a lineal energy range similar to the standard TEPC. Observing the spectral shape of the curve obtained with ΔV_{THGEM} value of 833 V, the lineal energy of this curve extends both to lower and higher values as compared to the standard TEPC. Furthermore, this curve also has a second small peak at the higher lineal energies. These changes of the spectral shape compared to the standard TEPC and the THGEM detector with $\Delta V_{THGEM} = 810$ V data were unexpected and the source of these results are unknown. A possible source as mentioned in *Section 5.3.2.* above is an uneven gain multiplication within the THGEM holes. Additional sources of this effect may also be present, especially since the data set at $\Delta V_{THGEM} = 810$ V did not present the same unexpected effects.

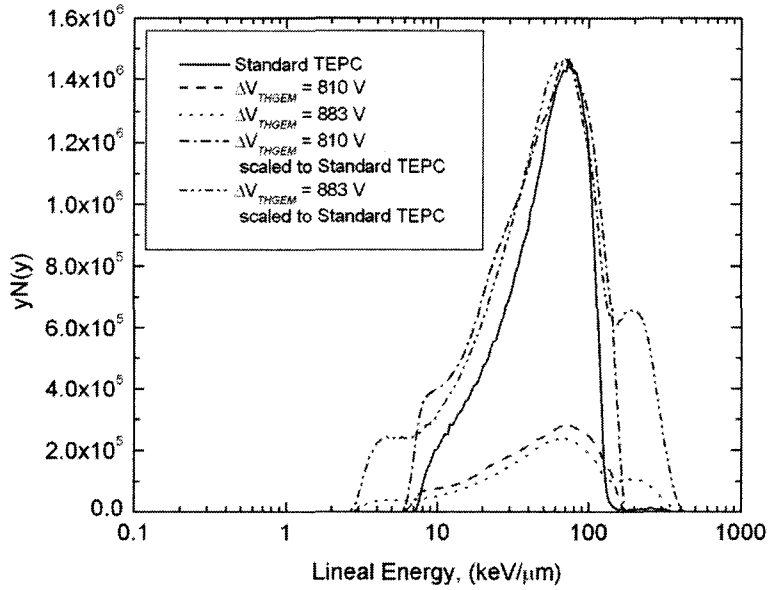

Figure 5.4: Comparison of spectra between the THGEM detector with THGEM B (0.40 mm insulator thickness) and the standard TEPC collected at E_p = 2.3 MeV. In order to compare the shape of the spectrum the THGEM detector spectrum (dash-dot curve) is normalized to the standard TEPC spectrum (solid curve). The shape of the THGEM detector curve obtained at ΔV_{THGEM} = 883 V (dotted curve) has a broader range than the other two curves presented and a second small peak at the higher lineal energies.

5.3.4 Measured Dose

The dose measured using the THGEM detector was obtained using the spectra presented in Figure 5.3 (a). The same calculations as described in Section 4.6 were used to analyze the data set obtained when THGEM B was used within the detector. Even though the thickness of THGEM B is greater than THGEM A, the sensitive volume is not affected since it is assumed the THGEM is not part of the radiation interaction region. Figure 5.5 displays the dose measured with the THGEM detector as a function of ΔV_{THGEM}. The mean measured dose rate with the THGEM detector (dash line) was 7.9 mGy/min at 150 μA with a standard

deviation of 0.5 mGy/min at 150 μA. The dose rate measured with the standard TEPC (solid line) using the same beam conditions was (6.9 ± 0.7) mGy/min at 150 μA. Between the two detectors a difference of 13 % was observed in the measured dose rate and the two measurements are within error. Compared to the small increasing trend observed with THGEM A (Figure 4.8), there is no obvious trend in the dose rate measured when THGEM B was used within the THGEM detector. One interesting observation of the measured dose rate with THGEM B, is the value is within error with the standard TEPC value whereas this result was not observed with THGEM A (Figure 4.8).

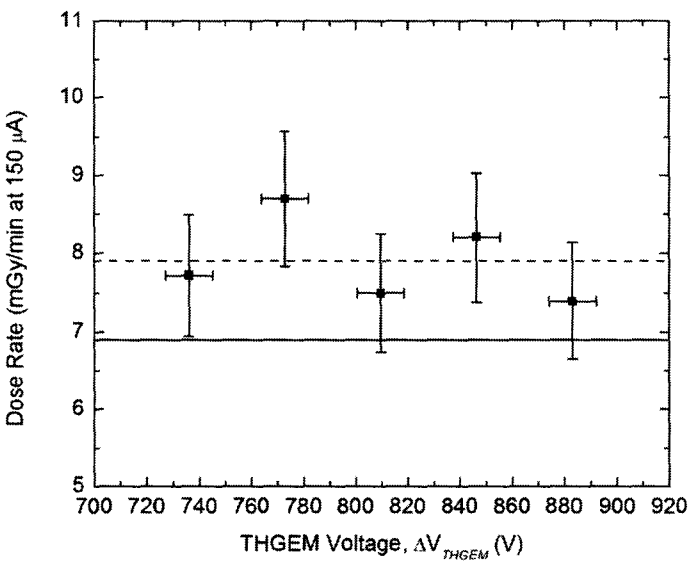

Figure 5.5: Measured dose rate with the THGEM detector using THGEM B (0.40 mm insulator thickness) and the dose rate measured by the standard TEPC. The data points correspond to the dose rate obtained from the spectra shown in Figure 5.3 (a). The dashed line is the mean value of the dose rate measured with the THGEM detector and the solid line represents the dose rate measured with the standard TEPC.

5.4 THGEM C: Insulator Thickness 0.70 mm

THGEM C was fabricated with an insulator thickness of 0.70 mm and placed within the THGEM detector assembly. The diameter and pitch of the THGEM holes remained the same as in THGEMs A and B. The value of R1 was 10 MΩ and three different R2 values were tested, 0.47 MΩ, 0.87 MΩ and 1 MΩ. Several experiments were conducted to observe the function of the THGEM detector containing THGEM C. The detector stability and reproducibility will be presented along with the attempt to measure the relative gain and the observed spectra as a function of R2.

5.4.1 Detector Stability and Reproducibility

The results obtained when THGEM C was used within the THGEM detector were unreliable. The stability tests were conducted with beam parameters of E_p = 2.1 MeV and I_p = 150 μA. The THGEM detector voltage settings were set at 100 V for ΔV_{Drift} and 1104 V for ΔV_{THGEM}. For conditioning purposes the detector voltages were left on throughout the entire 8 day time period, although the voltage across the THGEM was decreased between the daily measurements. A value of R2 = 0.87 MΩ was used for the stability study. (A value of 0.47 MΩ for R2 was tested prior to 0.87 MΩ but a signal from the detector was not observed.) Figure 5.6 is a graph of the measured count rate over a period of 8 days and the count rate was unstable with no observable trends. A couple of interesting observations include the data obtained on day 1 and day 8.

The data shown in Figure 5.6 for days 1 to 4 were obtained with amplifier gain of 100 x 0.7 while amplifier gain corresponding to the data for day 8 was reduced to 30 x 0.7 although the experimental conditions were the same for all 8 days. It appears that a conditioning time may be required before the THGEM electron multiplication becomes stable. After day 1, days 2, 3 and 4 have higher count rates than day 1, furthermore, by day 8 the gain was decreased in order to maintain the count rate within the same range as the previous days. This may imply that after 8 days of using the detector the rate increased and thus the gain had to be decreased to limit pulse saturation. The detector behaviour during the stability experiments was unexpected and further studies with THGEM C are required to understand the function better.

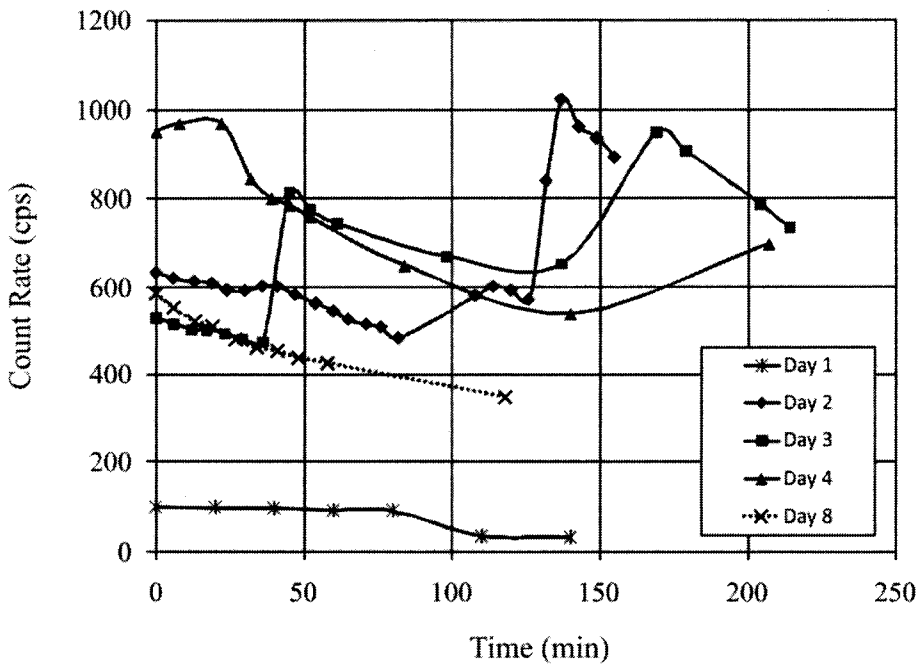

Figure 5.6: Systematic measurement of the count rate measured by the THGEM TEPC using THGEM C (0.70 mm insulator thickness). The CAS pulse processing system was used to acquire the gross count rate for a period of 5 minutes. Measurements were acquired at intervals of 5 minutes or greater.

5.4.2 Gas Multiplication

An attempt to measure the relative gain using THGEM C within the THGEM detector was conducted. During signal acquisition the beam parameters were set to $E_p = 2.3$ MeV and $I_p = 150$ μA, and the detector voltages were ΔV_{Drift} = 100 V and ΔV_{THGEM} ranged from 909 V to 1136 V. The resistor values R1 and R2 within the THGEM detector were 10 MΩ and 1 MΩ, respectively. Due to the unexpected spectral shape obtained the relative gain as a function of ΔV_{THGEM} was not possible. Figure 5.7 displays the microdosimetric spectra collected using

THGEM C. Although the spectral shape is not as expected, from the data displayed in Figure 5.7, the signal detected appears to be responding to the THGEM applied voltage.

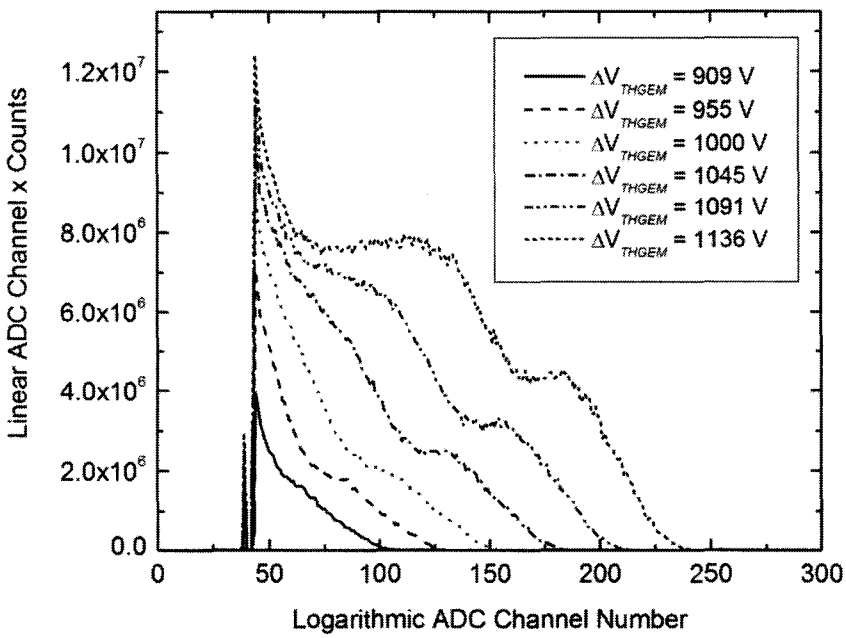

Figure 5.7: The microdosimetric spectra obtained with the THGEM detector using THGEM C (0.70 mm insulator thickness). The spectra do not resemble the expected microdosimetric spectrum and thus the relative gain was not measured. Although, from the data obtained, there is an increase in signal gain with increasing THGEM voltage, ΔV_{THGEM}.

5.4.3 Microdosimetric Spectrum

The microdosimetric spectrum obtained with THGEM C was not as expected and different shapes were obtained as shown in Figure 5.7. The spectral shape of the data displayed in Figure 5.7 does not correspond to the expected

curves as shown in Figures 4.6 and 5.4. A second attempt to obtain a microdosimetric spectrum using THGEM C was conducted. For this study the beam parameters were E_p = 2.1 MeV and I_p = 150 μA and THGEM detector voltages of ΔV_{Drift} = 100 V and ΔV_{THGEM} = 1104 V were applied. The resistor values R1 and R2 within the detector were 10 MΩ and 0.87 MΩ, respectively. Figure 5.8 displays the spectrum obtained with the standard TEPC using the same beam conditions and is compared to two spectra obtained with the THGEM detector using THGEM C. The spectral shapes presented in Figures 5.7 and 5.8 obtained with the THGEM detector are different. Although the beam energy is different between the two, ideally the spectral shapes should be similar. The one main difference between these two data sets is the value of R2 used in each experiment. For the data presented in Figure 5.7 a value of 1 MΩ was used for R2 to collect the spectra while a value of 0.87 MΩ was used for R2 in the data presented in Figure 5.8. The change in spectral shape observed between these two studies with THGEM C indicates the value of R2 may have a large influence on the collection of electrons after they emerge from the THGEM holes.

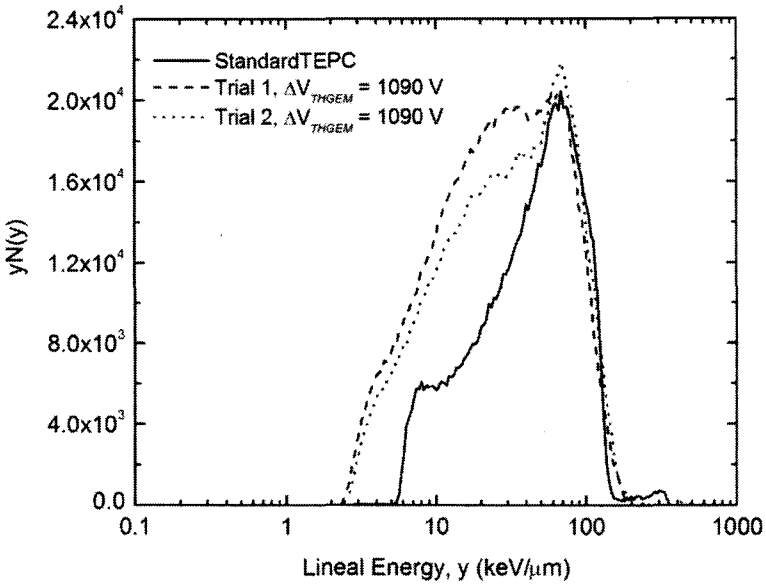

Figure 5.8: Microdosimetric spectra obtained with using THGEM C (0.70 mm insulator thickness) within the THGEM TEPC and compared to the standard TEPC spectrum. Data for both detectors were obtained using beam parameters: $E_p = 2.1$ MeV and $I_p = 150$ μA.

Looking at the THGEM spectra in Figure 5.8, the double peak along with the broadness of the peak is inconsistent with the microdosimetric spectrum obtained with the standard TEPC. The results obtained with THGEM C indicate that with increasing insulator THGEM thickness the detector function is no longer as consistent as observed when THGEMs A and B were used within the THGEM detector.

5.5 THGEM D: Insulator Thickness 1.48 mm

The last THGEM insulator thickness tested with the THGEM detector was 1.48 mm. As observed with THGEM C the results were not reliable and similarly THGEM D did not provide positive results. Furthermore, THGEM D contained

thicker copper (Cu) layers as compared to THGEMs A, B and C. This increase in the amount of Cu available during irradiation led to the activation of Cu-64 and interference with the data acquisition. Figure 5.9 displays the spectra acquired using THGEM D. Data were acquired using detector voltages of ΔV_{Drift} = 100 V and ΔV_{THGEM} = 924 V and beam parameters E_p = 2.1 MeV and I_p = 300 μA. During acquisition the RTS pulse processing displayed an unexpected spectral shape. As a result, the proton beam was turned off and the detector response was observed. As shown in Figure 5.9 additional signal was observed once the radiation field was terminated. Furthermore, the peak location was at a different location compared to the spectral shape obtained when the detector was exposed to the radiation field. The gamma ray component was obtained by reducing the beam proton energy to 1.8 MeV. Overall, the data presented in Figure 5.9 indicates an activation of a certain material within the THGEM detector. After careful handling of the detector, it was concluded the Cu layer of THGEM D was activated when it was exposed to neutrons. Once THGEM D was removed from the detector the count rate was monitored over two days and the decay rate indicated the Cu was activated to Cu-64 which has a half-life of 13 hours. Therefore, all subsequent THGEMs were always composed of the thinnest possible Cu layers to minimize the effects of Cu-64 activation.

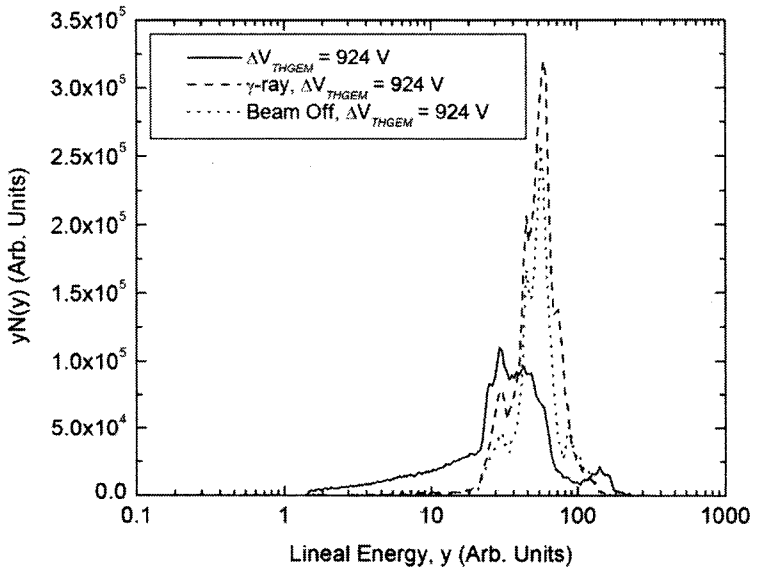

Figure 5.9: Microdosimetric spectra obtained using THGEM D (1.48 mm insulator thickness) within the THGEM detector. The thicker Cu layers of THGEM D led to the activation of Cu-64 during neutron irradiation. Furthermore, the spectrum obtained with the THGEM detector does not resemble the expected microdosimetric spectrum obtained when exposed to the mixed radiation field. Also, the detector was responding to the internal activation of the THGEM which is depicted by the dotted curve.

5.6 Discussion

Along with THGEM A presented in Chapter 4, the THGEM TEPC was also tested with three additional THGEM insulator thicknesses of 0.40 mm, 0.70 mm and 1.48 mm. During these experiments the results indicated with increasing insulator thickness of the THGEM the detector function degraded. The results obtained with THGEM B (0.40 mm insulator thickness) were consistent and provided similar results to THGEM A. The studies relating to stability, relative gain, microdosimetric spectrum and measured dose rate obtained with THGEM B were presented and compared to THGEM A. The behaviour of THGEM B was

not as stable as THGEM A but the overall performance was as expected. The discrepancy of the dose comparison of THGEM A and THGEM B with the standard TEPC will be further discussed in Chapter 6. As the insulator thickness of the THGEM increased to 0.70 mm (THGEM C) and 1.48 mm (THGEM D) the detector function degraded. The detector function when THGEM C was used indicates a dependence on the R2 value as different spectral shapes were observed as shown in Figures 5.7 and 5.8. In either case the spectral shape was not similar to the expected shape as obtained with the standard spherical TEPC. Finally THGEM D provided additional insight on the THGEM fabrication and the thickness of the conducting copper layers of the THGEM. An increase in the thickness of the copper layers above and below the insulator of the THGEM led to the neutron activation of Cu-64 which affects the measured spectra as shown in Figure 5.9. From this study it was realized that the copper layers of the THGEM must be kept to a minimal thickness to minimize the activation of Cu and interference with the measured microdosimetric spectra and dose of interest.

Although the results obtained with THGEMs B, C and D varied, each THGEM insulator thickness and fabrication provided additional information on the THGEM detector function. During these studies it was also observed the value of R2 used within the detector does affect the signals detected and further studies to determine the optimal value for a given insulator thickness are required.

Chapter 6

Discussion & Conclusions

6.1 Discussion

The detector based on the THGEM for microdosimetry was successfully constructed and investigated. Throughout the fabrication process of the THGEM foils, the assembly of the detector and the conducting of experiments a large insight on the detector function was obtained. The detector was exposed to a mixed (n,γ) radiation field and the microdosimetric spectrum was collected. For the THGEM foils with insulator thicknesses of 0.12 mm and 0.40 mm the expected spectrum was observed, while for the THGEMs with insulator thickness of 0.70 mm and 1.48 mm the spectra measured did not resemble the expected microdosimetric spectra.

Development of the THGEM TEPC has led to a better understanding of the detector design and its capabilities. From the investigations conducted with the THGEM detector additional knowledge on the function and relevant parameters was obtained. Due to the many available parameters associated with the detector, conducting systematic experiments was difficult. Additionally, as

the lithium target is exposed to protons over long periods of time the radiation field generated can weaken. Although these changes are small, when trying to understand the THGEM detector function it is hard to distinguish if the effects are due to the detector or to the radiation field used to expose the detector when comparing data obtained over a long period of time. The target can be restored, which maximizes the generated neutron field but with use it continually weakens, especially when it is exposed to high proton currents. In the research presented here the main variables tested were the THGEM thickness and the voltage bias, ΔV_{THGEM} while trying to keep all other variables constant. An unexpected variable due to the THGEM thickness also led to changes in the $R2$ value. Additionally, every time the detector had to be disassembled and reassembled the detector components had to be cleaned and the chamber had to be re-filled with TE gas. Although all processes were conducted systematically every time the detector was reassembled, it was hard to maintain all the variables not being investigated consistent. Many challenges were encountered and some were overcome and others have led to additional enquiries and require further investigations to understand the detector function better. Overall, the THGEM detector provided promising results and additional research to develop the THGEM TEPC further should be conducted. In this Chapter the interesting, important and unexpected observations, methods to improve the THGEM detector function along with future research will be discussed.

6.1.1 Detector Components and Physical Dimensions

As presented in Section 1.6 the versatility and robustness of the THGEM are attractive features for a detector component. The design of the THGEM TEPC presented in Section 2.3 is a prototype and was built to allow for additional sensitive volumes and THGEM holes to be incorporated to create a two-dimensional position sensitive detector. This design of the detector would allow for two dimensional dose maps to be generated. To create a miniature detector using the design described in Section 2.3 the components can be made smaller. The A-150 and rexolite TE layers can be decreased in dimensions to encompass the sensitive volume and limit the additional area required for fabrication. Similarly, the actual size of the THGEM shown in Figure 2.3 can be significantly reduced to a surface area slightly greater than the cross section area of the sensitive volume. Furthermore, the sensitive volume can be decreased to detect higher dose rates such as those encountered in radiation therapy. Using right cylindrical geometry allows for easy fabrication of smaller sensitive volumes. Compared to the standard 0.5 inch TEPC which has a sensitive volume of 1073 mm^3, the THGEM detector as described in Section 2.3 has a sensitive volume of 98 mm^3. By further decreasing the sensitive volume, even higher event rates should be detected.

In the studies presented in Chapters 4 and 5 the hole diameter and pitch of the THGEMs was maintained the same for all insulator thicknesses tested.

Simulations of the avalanche gain as a function of hole diameters were conducted and are presented in Byun *et al.* (2009). The hole diameters simulated were: 0.3 mm, 0.6 mm and 0.9 mm for insulator thicknesses of 0.6 mm and 0.9 mm (Byun, 2009). It was noted the larger the hole diameter, the higher the voltage required to obtain the same gain. Given the versatility of the THGEM and simple fabrication process of the THGEM, it may be beneficial to investigate and optimize the size of the THGEM hole diameter as a function of voltage experimentally. According to Breskin *et al.* (2009) the larger hole diameter of the THGEM as compared to the GEM allows for a more effective electron collection and transmission of the electrons through the THGEM holes. As a result optimizing the hole diameter of the THGEM will increase the detector efficiency and may lead to higher detector gains. By using several THGEM elements in cascade even higher detector gains at lower ΔV_{THGEM} values per THGEM can be obtained and lead to higher operational stability (Breskin, 2009). Given that the stability of the THGEMs tested deteriorated with increasing THGEM thickness, optimizing the hole diameter of the THGEM as a function of thickness may provide a stable THGEM. Etching of the copper away from the THGEM holes also reduces edge discharges and results in higher gains (Breskin, 2009). Thus, optimizing the rim size along with the THGEM hole diameter should minimize the breakdown probability of the THGEM detector. Finally, the conducting layers of the THGEM should be kept to a minimum thickness to avoid activation

of the material, as was observed with the copper layers of THGEM D (1.48 mm insulator thickness).

Breakdown of the detector was observed many times during the investigations presented in Chapters 4 and 5. Breakdown is the result of charge build up on exposed insulator surfaces within the detector, such as the THGEM foil, which breaks down and the charge drains off (Braby, 1995). Breakdowns became more frequent with increasing THGEM insulator thickness due to the higher voltage values applied to the detector. In some cases when the THGEM was checked under a microscope after breakdown a black substance (char) could be seen around and within one or two of the THGEM holes, indicating a discharge occurred through those holes. Sometimes, no visible effects of breakdown could be observed on the THGEM. All THGEMs were re-etched after breakdown to clean the THGEM holes and they were then reused within the detector.

The values of $R1$ and $R2$ used to divide the voltage between the THGEM holes and the collection plate (refer to Figure 2.2) provide the ability to adjust how the applied voltage (HV2) is distributed between ΔV_{THGEM} and ΔV_{CP} (see equations (2.2) and (2.3)). The value of $R1$ was set at 10 MΩ and the value of $R2$ ranged between 0.47 – 1.33 MΩ. Keeping $R2$ around a tenth of $R1$ ensures the voltage divider provides ΔV_{THGEM} with the required high bias to generate electron multiplication and the remaining portion of the voltage is used to bias the

collection plate and guide the emerging electrons from the bottom of the THGEM holes towards the anode. It was observed with THGEM C when the value of 0.47 MΩ was used for $R2$ no signal was collected from the detector. It was assumed the electric field between the bottom of the THGEM holes and the anode was not strong enough to pull the emerging electrons from the THGEM and thus no signal was detected. As the value of $R2$ was increased to 0.87 and 1 MΩ a signal with THGEM C was observed with the THGEM detector. Therefore, the value of $R2$ as a function of THGEM thickness should be optimized to ensure electron collection by the anode is achieved.

6.1.2 Interesting and Unexpected Data with the THGEM TEPC

During experiments and data acquisition unexpected effects were observed. Two of the most common events included the breakdown of the detector and the signal polarity associated with the preamplifier signal. These were independent effects which occurred frequently but sometimes the incidence of breakdown led to a signal polarity change. A static electric field due to the build up of charges near the THGEM holes and after a breakdown was generated a reverse in the signal polarity was observed. Furthermore, when a static electric field was created, pulses were detected by the preamplifier even when the proton beam current was turned off. This was an unexpected effect and was only noticed when the proton beam was turned off and the detector high voltages were set to 0 V, yet pulses were still observed on the oscilloscope. The reversal in signal

polarity was unexpected and initially led to confusion between the detection of actual radiation-induced events and internal events generated due to the charge build up from the detector breakdown. Interestingly, although a polarity reversal was induced and a static electric field generated after a breakdown, the detector still responded to the radiation field.

The microdosimetric spectral pattern obtained with the THGEM detector was compared with the standard TEPC. Comparable spectra were obtained with THGEM A (0.12 mm insulator thickness) and THGEM B (0.40 mm insulator thickness). The spectra with THGEM A thickness within the detector were obtained with two different THGEMs (refer to Figure 4.7). The two spectra were comparable with the standard TEPC spectrum but the shape between the two THGEMs does vary. The spectrum shown in Figure 4.7 (a) correlates very well with the spectrum of the standard TEPC, whereas the spectrum obtained with the second THGEM tested (Figure 4.7 (b)) has a larger deviation from the standard TEPC spectral shape. Two obvious observations in Figure 4.7 (b) are the second small peak observed at the high lineal energies and the low lineal energy cut-off compared to the standard TEPC. Since two different THGEMs were used for the data presented in Figure 4.7, the difference between the two spectral shapes may be related to the THGEM fabrication and/or function. The spectral shape of the THGEM detector with THGEM B (0.40 mm insulator thickness) was also compared to the standard TEPC (see Figure 5.4). The THGEM spectral shape in

Figure 5.4 also contains a small second peak similar to the spectral shape of the THGEM A spectrum shown in Figure 4.7 (b). This is an interesting observation indicating the cause of the second peak may not be solely related to the THGEM.

Additionally, the dose rate was calculated from the data acquired with the THGEM detector with the THGEM thicknesses of THGEM A (0.12 mm insulator thickness) and THGEM B (0.40 mm insulator thickness). In Figures 4.7 and 5.5 the measured dose rate with the THGEM detector and the standard TEPC is presented. The measured dose rate was 6.4 ± 0.1 mGy/min with THGEM A and 7.9 ± 0.5 mGy/min with THGEM B. Even though the same beam proton energy and current parameters were used to generate the radiation field being measured, comparing the two THGEM detector dose rates is not valid. Fluctuations in the radiation field over time does occur as described at the beginning of Section 6.1 and thus the difference in the two measured dose values with the THGEM detector may be due to the radiation field and/or to the actual THGEM detector, and cannot be deciphered. In order to further examine the measured dose of the THGEM detector as a function of THGEM thickness a neutron monitoring counter should be used to normalize the effects of the radiation field. Furthermore, when comparing the dose rate measured with the THGEM to the standard TEPC, the sensitive volumes of both detectors should be exposed to the same field. In the measurements presented here, both detectors were centred on the beam target as precisely as possible, but due to the different shape of the two

detectors and sensitive volume size ensuring the two detectors were exposed to the same field was difficult. It was shown by Byun *et al.* (2007a) the dose as a function of axial distance from the centre of the lithium target can very up to approximately 20 % over a distance of 3 cm. Thus the measured dose rate between the THGEM detector and the standard TEPC can vary up to 20 % based only the position of each detector relative to the target.

6.1.3 Preparation of the THGEM Detector

Prior to testing the THGEM detector certain procedures are followed. Once the detector is thoroughly cleaned, assembled and the outside air is removed the detector must be filled with TE propane gas at the desired pressure. The method used for gas filling involved a timer rather than a pressure gauge. This method was used because the available pressure gauge can only measure the pressure up to 100 torr. Since the data presented in Chapters 4 and 5 mainly required a pressure of 167 torr, a relationship between the time required to raise the pressure by a certain amount was used to extrapolate to the desired pressure. Although this method was consistently used every time the detector was filled, there is an error associated with the uncertainty of operating the timer and controlling the air flow when filling the detector. The error of ± 5 torr within the desired pressure measurement was used to estimate the uncertainty associated with the gas filling technique. Obviously, for lower gas pressures, the gauge is used to obtain the desired pressure, but since the operator still has to adjust the air

flow and turn it on and off, the uncertainty of ± 5 torr was maintained for all pressure measurements.

Once the THGEM detector is filled to the required pressure the detector is ready for testing. Conditioning involved applying the high voltages, HV1 and HV2, to the detector a certain amount of time prior to exposure to radiation. According to Braby *et al.* (1995) conditioning of a new detector is not uncommon and generally involves maintaining the detector under vacuum for a couple of days followed by application of voltage for a few hours prior to using the detector. The THGEM detector was always maintained under vacuum for at least one day prior to filling with TE gas and voltage conditioning. The conditioning period was varied from a few hours to over a day. A consistent conditioning procedure was not achieved. In some instances it was found a short conditioning time was required prior to using the detector. Overall, every time the detector was reassembled and refilled with TE propane gas, the HV supplied to the detector was introduced slowly and increased to the required values prior to exposure to radiation. After conditioning the detector, the voltages were adjusted as required for the experiments being conducted. It would be interesting to investigate if the insulator thickness of the THGEM has an effect on the conditioning time of the detector.

6.2 Future Work

The investigations presented in this thesis provided a foundation on the THGEM TEPC. The results have indicated the detector function is feasible as a TEPC but further studies are required to optimize the detector performance. Future work directly arising from the research presented here includes investigating the THGEM performance as a function of hole diameter and thickness, optimizing R1 and R2, understanding the breakdown limits of the detector bias, ΔV_{THGEM} and optimizing the drift field, ΔV_{Drift}. A significant improvement to the current detector design is the addition of a calibration source within the detector. This would ensure an independent and consistent calibration method of lineal energy.

Additional future work should include investigations of smaller sensitive volume and fabrication of a miniature detector. It would also be interesting to investigate the detector performance with several THGEM elements in a cascade and expansion of the current detector design into a two-dimensional imaging device.

6.3 Conclusion

The THGEM TEPC was designed, fabricated and tested with a mixed (n,γ) radiation field. Two of the main goals were to observe a signal followed by a microdosimetric spectrum with the THGEM detector. These two objectives

were realized, which led to additional studies to improve the detector performance further. The THGEM electron multiplication as a function of voltage bias and insulator thickness was studied, and the spectra and measured dose rate obtained with the THGEM detector were compared with the standard TEPC. The results of all the studies led to the following conclusions: (1) THGEM detector can function as a TEPC, (2) the expected gain relationship of the THGEM foil was observed, (3) the measured spectra and dose using the THGEM detector are comparable to the standard TEPC, (4) the THGEM detector can function at various TE gas pressures and thus simulate smaller tissue sizes (< 2 μm diameter right cylindrical volumes) and (5) the insulator thickness of the THGEM foil does affect the detector function. Further studies with the THGEM TEPC are required and should be conducted to develop the THGEM TEPC further. As shown in these initial experimental studies, the THGEM TEPC is a promising detector for microdosimetry and the versatility of the THGEM foil along with the simple design and cost effective fabrication of the detector are attractive features for further development.

Appendix

Calibration of Microdosimetric Spectrum

A.1 Introduction

As described in Section 3.5 the data collected by the pulse processing systems (CAS, DPP and RTS) are distributed as a pulse-height spectrum. In order to convert the data to the calibrated microdosimetry spectrum the storage bins (each bin labelled by a Channel Number) used to collect the detector pulses must be converted to lineal energy. This process is accomplished by using a pulse generator and a known lineal energy associated with the spectrum or internal calibration source of the detector. In this Appendix, data obtained with the spherical TEPC will be used to describe the calibration process with the CAS. The calibration steps are the same for all three systems.

A.2 Calibration of Data Acquired with the CAS

For CAS the software Gammavision was used to collect the data and created a pulse-height spectrum. The horizontal axis represents the pulse amplitude of the signal and is labelled as Channel Number while the vertical axis stores the number of counts generated corresponding to each Channel Number.

Figure A.1 is a picture of a raw spectrum displayed by Gammavision acquired with the CAS.

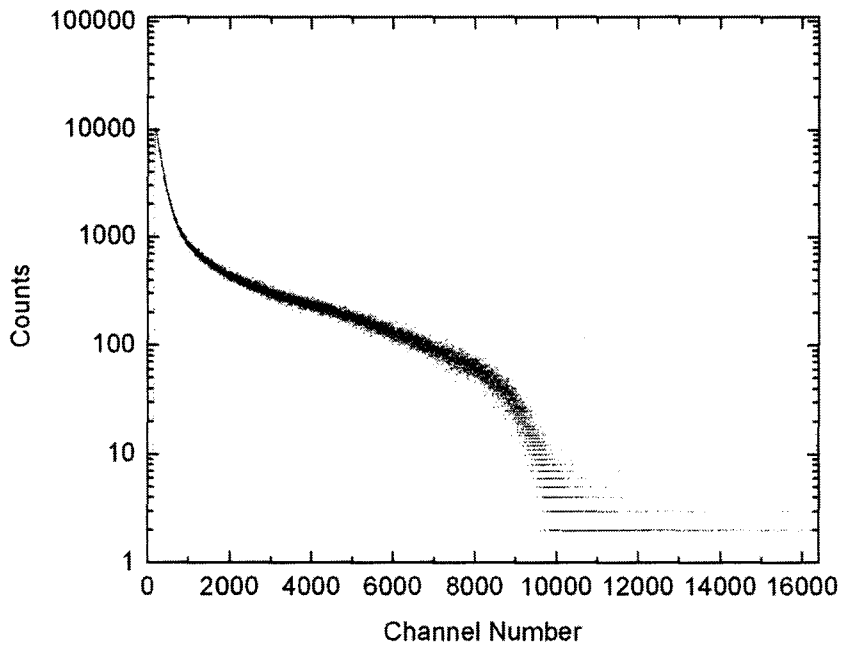

Figure A.1: Pulse height spectrum generated by Gammavision using the CAS pulse processing system.

Once the spectrum is acquired, the first step is to convert the channel number of the horizontal axis to pulse amplitude in Volts. This is conducted by using a pulser and generating a calibration curve. Figure A.2 displays the graph of the channel number to pulse amplitude calibration. A linear fit to the data provides the equation required to convert all channel numbers to pulse amplitude.

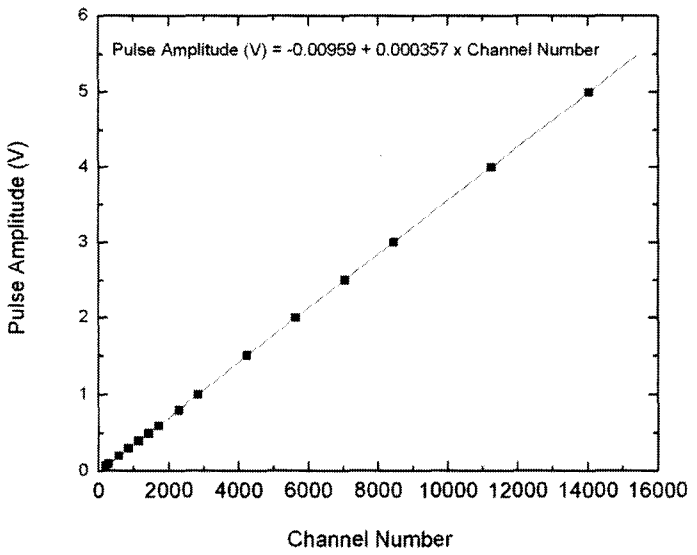

Figure A.2: The Calibration curve used to convert the Channel Number of the pulse height spectrum to the corresponding amplitude. A linear fit to the data allows for conversion of all channel numbers to amplitude in volts.

Using the internal alpha source of the spherical TEPC the corresponding channel number of the alpha peak is noted and converted to the corresponding pulse amplitude using the linear fit of the calibration curve shown in Figure A.2. Once the pulse amplitude corresponding to the alpha peak is acquired the conversion of all pulse amplitudes to lineal energy is carried out using the following factor:

$$y_i = PA_i\left(\frac{127}{PA_{127}}\right) keV/\mu m \qquad \text{(A.1)}$$

where PA_i corresponds to the pulse amplitude of channel i, PA_{127} is the pulse amplitude of the alpha peak and 127 is the lineal energy in keV/μm of the internal curium alpha source in the spherical TEPC. This step converts the channel

number of the pulse height spectrum shown in Figure A.1 to lineal energy, y_i. The next step is to redistribute the data in bins of decades. A conversion program is used to redistribute the number of counts into logarithmic bins. This generated a redistributed spectrum with data sorted into two columns, y_i and counts, $N(y_i)$. Plotting the data with y_i on a logarithmic scale on the horizontal axis and the counts $N(y_i)$ on the vertical axis. Figure A.3 is a plot of the data shown in Figure A.1 after conversion to lineal energy and redistribution.

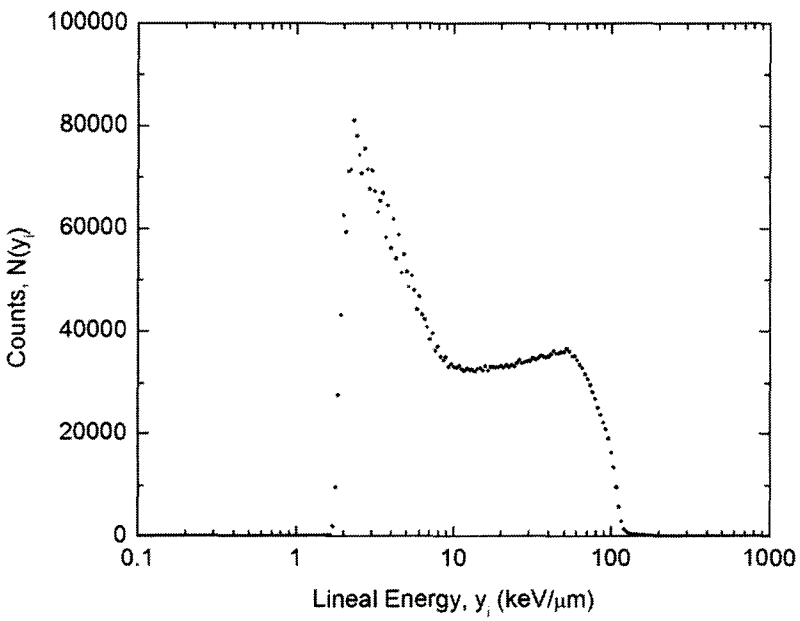

Figure A.3: Spectrum of data presented in Figure A.1 after lineal energy calibration and redistribution.

The final step to generate the standard representation of the microdosimetric spectrum is to display *yN(y)* on the vertical axis. This is obtained by multiplying the lineal energy of each bin with the corresponding number of counts in that bin. The final spectrum generated is shown in Figure A.4.

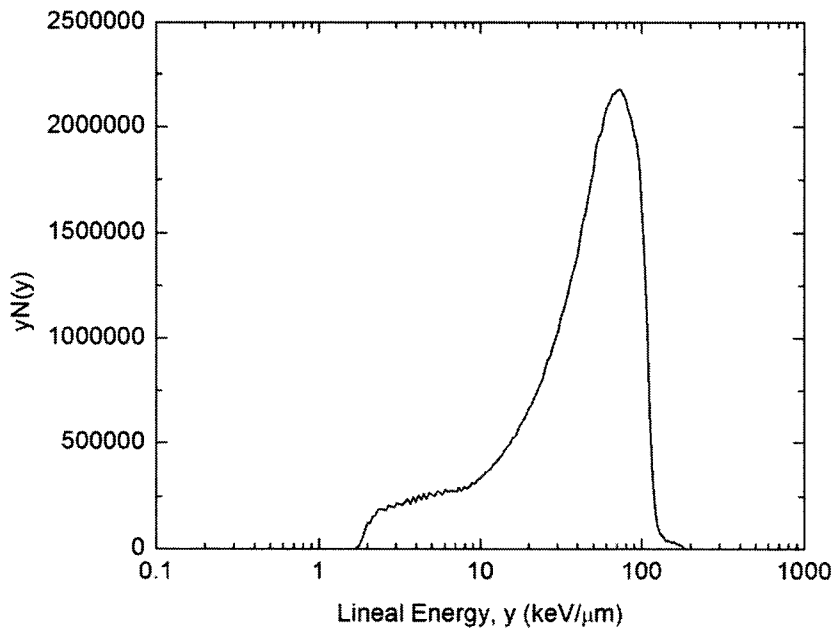

Figure A.4: The standard representation of the microdosimetric spectrum obtained after calibration of the data collected shown in Figure A.1.

Once the data are calibrated and displayed as shown in Figure A.4, the area under the curve is related to the absorbed dose within the sensitive volume of the detector and is used to calculate the absorbed dose in the microscopic tissue volumes being simulated by the detector.

Bibliography

Bateman, S.N., A. Pejović-Milić, I.M. Stronach, F.E. McNeill, and D.R. Chettle, 2000. "Performance appraisals of digital spectroscopy systems for the measurement of bone lead," *Appl. Rad. Isot.* **53(4-5):** 647-640.

Braby, L.A., G.W. Johnson and J. Barthe, 1995. "Practical considerations in the design and construction of tissue-equivalent proportional counters," *Radiat. Prot. Dosim.* **(61)4:** 351-379.

Breskin, A., R. Alon, M. Cortesi, R. Chechik, J. Miyamoto, V. Dangendorf, J.M. Maia, J.M.F Dos Santos, 2009. "A concise review on THGEM detectors," *Nucl. Instrum. Methods A.* **598:** 107-111.

Byun, S.H., A. Pejović-Milić, S. McMaster, W. Matysiak, Aslam, Z. Liu, L. Watters, W. V. Prestwich, F. E. McNeill and D. R. Chettle, 2007a. "Dosimetric characterization of the irradiation cavity for accelerator based in vivo neutron activation analysis," *Phys. Med. Biol.* **52(6):** 1693-1703.

Byun, S.H., K. Chin, W. V. Prestwich, Z. Liu, and S. Saxena, 2007b. "Development of a pulse processing system for real-time analysis of microdosimetic spectra," *Nucl. Instr. Methods A* .**579(1):** 256-259.

Byun, S.H., G.M. Spirou, A. Hanu, W.V. Prestwich and A.J. Waker, 2009. "Simulation and first test of a microdosimetric detector based on a thick gas electron multiplier," *IEEE Trans. Nucl. Sci.* **56(3):** 1108-1113.

C-Lec Plastic Inc. "Welcome to C-LEC Plastics!!" *http://www.rexolite.com*. (14 September, 2010)

Chadwick, M.B, H.H. Barschall, R.S. Caswell, P.M. DeLuca, G.M. Hale, D.T.L. Jones, R.E. MacFarlane, J.P. Meulders, H. Schuhmacher and U.J. Schrewe, A. Wambersie, P.G. Young, 1999. "A consistent set of neutron kerma coefficients from thermal to 150 MeV for biologically important materials," *Med.Phys.* **26(6):** 974-991.

Chechik, R., A. Breskin, C. Shalem, D. Mörmann, 2004. "Thick gem-like hole multipliers: properties and possible applications." *Nucl. Instrum. Methods A.* **535:** 303-308.

Chechik, R., A. Breskin, C. Shalem, 2005. "Thick gem-like multipliers-a simple solution for large area uv-rich detectors." *Nucl. Instrum. Methods A.* **553:** 35-40.

Cortesi, M., R. Chechik, A. Breskin, G. Guedes, V. Dangendorf, D. Vartzky, D. Bar, 2007. "Advances in imaging THGEM-based detectors." *Nucl. Instrum. Methods A.* **572:** 175-176.

Di Mauro, D., B. Lund-Jensen, P. Martinengo, E. Nappi, R. Oliveira, V. Peskov, L. Periale, P. Picchi, F. Pietropaolo, I. Rodionov, J.C. Santiard, 2007. "Development of innovative micro-pattern gaseous detectors with resistive electrodes and first results of their applications." *Nucl. Instrum. Methods A.* **581:** 225-231.

Dubeau, J., A.J. Waker, M. Biggar, M.D. Rayner, E.W. Sommerville, S.E. Welch, 2000. "Dosimetric response to γ rays and neutrons of a tissue-equivalent microstrip gas counter." *Radiat. Prot. Dosim.* **91(4):** 391-401.

Dubeau, J. and A.J. Waker, 2008. "Neutron microdosimetric response of a gas electron multiplier." *Radiat. Prot. Dosim.* **128(4):** 413-420.

Farahmand, M., A.J.J. Bos, J. Huizenga, L.D. Nardo, C.W.E. van Eijk, 2003. "Design of a new tissue-equivalent proportional counter based on a gas electron multiplier." *Nucl. Instrum. Methods A.* **509:** 262-267.

Farahmand, M., A.J.J. Bos, L. De Nardo, C.W.E. van Eijk, 2004. "First microdosimetric measurements with a TEPC based on a GEM." *Radiat. Prot. Dosim.* **110(1-4):** 839-843.

Langen, K.M., P.J. Binns, A.J. Lennox, T.K. Kroc, P.M. DeLuca Jr., 2002. "Pileup correction of microdosimetric spectra", *Nucl. Instrum. Methods A.* **484:** 595-612.

Gerdung, S., P. Pihet, J.E. Grindborg, H. Roos, U.J. Schrewe and H. Schuhmacher, 1995. "Operation and application of tissue equivalent proportional counters", *Radiat. Prot. Dosim.* **61(4):** 381-404.

Hall, E.J. and A.J. Giaccia, 2006. *Radiobiology for the Radiologist, 6th ed.* Philadelphia: Lippincott, Williams and Wilkins.

ICRU, 1983. *Microdosimetry ICRU Report 36.* Bethesda: ICRU Publications.

Kliauga, R., A.J. Waker and J. Barthe, 1995. "Design of tissue-equivalent proportional counters", *Radiat. Prot. Dosim.* **61(4):** 309-322.

Knoll, G.F., 2000. *Radiation Detection and Measurement, 3rd ed.* New Jersey: John Wiley & Sons, Inc.

Lee, C.L. and X.-L. Zhou, 1999. "Thick target neutron yields for the 7Li(p,n)7Be reaction near threshold," *Nucl. Instr. and Meth. B.* **152(1):** 1-11.

Matysiak, W., W.V. Prestwich and S.H. Byun, 2008. "Measurement of the thick target 7Li(p,n) neutron source spectrum using a 3He ionization chamber," *Nucl. Instr. and Meth. A.* **592:** 316-324.

Oed, A., 1988. "Position-sensitive detector with microstrip anode for electron multiplication with gases." *Nucl. Instr. And Meth. A.* **263:** 351-359.

Oliveira, R., V. Peskov, F. Pietropaolo, P. Picchi, 2007. "First tests of thick GEMs with electrodes made of a resistive kapton." *Nucl. Instrum. Methods A.* **576:** 362-366.

Ostling, J., A. Brahme, M. Danielsson, T. Francke, C. Iacobaeus, V. Peskov, 2003. "Study of hole-type gas multiplication structures for portal imaging and other high count rate applications." *IEEE Trans. Nucl. Sci.* **50:** 809-819.

Periale, L., V. Peskov, P. Carlson, T. Francke, P. Pavlopoulos, P. Picchi, F. Pietropaolo, 2002. "Detection of the primary scintillation light from dense Ar, Kr and Xe with novel photosensitive gaseous detectors." *Nucl. Instrum. Methods A.* **478:** 377-383.

Periale, L., V. Peskov, P. Carlson, C. Iacobeause, T. Francke, N. Pavlopoulos, F. Pietropaolo, T. Sokolova, P. Picchi, 2003. "Evaluation of various planar gaseous detectors with CsI photocathodes for the detection of primary scintillation light from noble gases." *Nucl. Instrum. Methods A.* **497:** 242-248.

Peskov, V., B. Baibussinov, S. Centro, A. Di Mauro, B. Lund-Jensen, P. Martinengo, E. Nappi, R. Oliveira, F. Pietropaolo, P. Picchi, L. Periale, I. Rodionov, and S. Ventura, 2007. "Development and First Tests of GEM-Like Detectors With Resistive Electrodes." *IEEE Trans. Nucl. Sci.* **54:** 1784-1791.

Reguigui, N., J. Morel, H. B. Kraiem, and A. Mahjoub, 2002. "Characterization of three digital signal processor systems used in gamma ray spectrometry," *Appl. Rad. Isot.* **56(1-2):** 93-97.

Rossi, H.H. and M. Zaider, 1996. *Microdosimetry and Its Applications*. Berlin: Springer-Verlag.

Sakurai, H., T. Tamura, S. Gunji, M. Noma, 1996. "A new type of proportional counter using a capillary plate." *Nucl. Instrum. Methods A.* **374:** 341-344.

Sauli, F., 1997. "Gem: A new concept for electron amplification in gas detectors." *Nucl. Instrum. Methods A.* **386:** 531-534.

Scates, D. M., and J. K. Hart, 2005. "A comparison of the high count-rate performance of three commercially available digital signal processors," *Appl. Rad. Isot.* **63(4):** 465-473.

Shalem, C., R. Chechik, A. Breskin, K. Michaeli, 2006a. "Advances in thick GEM-like gaseous electron multipliers-part I: atmospheric pressure operation." *Nucl. Instrum. Methods A.* **558:** 475-489.

Shalem, C., R. Chechik, A. Breskin, K. Michaeli, N. Ben-Haim, 2006b. "Advances in thick GEM-like gaseous electron multipliers Part II: Low-pressure operation." *Nucl. Instrum. Methods A.* **558:** 468-474.

Spirou, G.M., S.-H. Byun, and W.V. Prestwich, 2008. "Comparison of Three Pulse Processing Systems for Microdosimetry." *IEEE Trans. Nucl. Sci.* **55(5):** 2621-2626.

Vo, D.T. and P.A. Russo, 2002. "Comparison of the portable digital spectrometer systems," LA-13895-MS, Los Alamos National Laboratories.

Waker, A.J., 1995. "Principles of Experimental Microdosimetry." *Radiat. Prot. Dosim.* **61(4):** 297-308.